A Tale of Two Trees: Modeling Apical and Basal Tree Contribution to L2/3 V1 Pyramidal Cell Orientation Selectivity

Konstantinos-Evangelos Petousakis[1,2,*], Jiyoung Park[3,*], Athanasia Papoutsi[1], Stelios Smirnakis[3], Panayiota Poirazi[1,+]

[1]IMBB, FORTH, Heraklion, Crete, 70013, Greece

[2]Department of Biology, University of Crete, Heraklion, Crete, 70013, Greece

[3]Department of Neurology, Brigham and Women's Hospital and Jamaica Plain Veterans Administration Hospital, Harvard Medical School, Boston, MA, USA

+Corresponding Author: poirazi@imbb.forth.gr

[*]These authors contributed equally to this work

Pyramidal neurons, a mainstay of cortical regions, receive a plethora of inputs from various areas onto their morphologically distinct apical and basal trees. Both trees differentially contribute to the somatic response, defining distinct anatomical and possibly functional sub-units. To elucidate the contribution of each tree to the encoding of visual stimuli at the somatic level, we modeled the response pattern of a L2/3 V1 pyramidal neuron to orientation-tuned synaptic input. Towards this goal, we used a morphologically detailed computational model of a single cell, validated against electrophysiological and two-photon imaging data. Our simulations predict a synergistic effect of apical and basal trees on somatic action potential generation: basal tree activity, in the form of either depolarization or dendritic spiking, is necessary for producing somatic activity, despite the fact that most somatic spikes are heavily driven by apical dendritic spikes. This model provides evidence for synergistic computations taking place in the basal and apical trees of the L2/3 V1 neuron and emphasizes the potential role of predictive and attentional feedback input in these cells.

1. Introduction

In the primary visual cortex (V1), layer 2 and 3 (L2/3) pyramidal neurons conform to a stereotypical morphology characterized by separate apical and basal dendritic arbors. The apical tree consists of a thick apical trunk that extends into L1 and splits into an apical tuft. The basal tree consists of numerous dendritic segments, the majority of which sprout directly from the base of the soma, indicating that they can directly influence somatic output (Spruston, 2008). This compartmentalization of V1 neurons is also evident in the wiring diagram describing each tree: layer 4 (L4) and L2/3 pyramidal neurons synapse with basal dendrites of L2/3 pyramidal neurons, providing them with feedforward input (Coogan & Burkhalter, 1990; Larkum, 2013). The apical dendrites of the L2/3 pyramidal neurons instead receive feedback input from higher order areas of the cortex (such as the secondary and tertiary visual cortices, lateromedial area and prefrontal cortex (Coogan & Burkhalter, 1990; Larkum, 2013), as well as orientation-tuned thalamocortical input (Chen et al., 2013; Cruz-Martín et al., 2014; Jia et al., 2010; Roth et al., 2015). These anatomical and connectivity features of the apical and basal trees, complemented by their distinct biophysical properties (Cho et al., 2008), shape both the local dendritic processing and the integration of the two input streams at the soma.

Few studies have undertaken the technically difficult task of measuring single spine tuning properties in the mouse visual cortex (Chen et al., 2013; Iacaruso et al., 2017; Jia et al., 2010). These studies have shown that single spines of L2/3 pyramidal neurons exhibit orientation selectivity, with synaptic orientation preferences varying even on the same branch (Iacaruso et al., 2017; Jia et al., 2010). These findings raise the question of how dendritic integration of sparse synaptic inputs along the apical and basal trees shape orientation tuning in L2/3 V1

pyramidal neurons. In vitro studies have revealed multiple non-linear dendritic properties of synaptic integration, including active dendritic spikes, the backpropagation of action potentials, and dendritic properties of coincidence detection (Larkum, 2013; Palmer et al., 2014; Shai et al., 2015; Smith et al., 2013). These dendritic non-linearities augment the repertoire of single neuron computations (Poirazi et al., 2003; Poirazi & Papoutsi, 2020; Silver, 2010). Focusing on L2/3 V1 pyramidal neurons, it has been found that individual dendritic segments of L2/3 neurons generate activity independently of the soma, making their exact contribution to somatic output unclear (Palmer et al., 2014; Smith et al., 2013). This could indicate that multiple dendritic segments need to be activated in order to generate a spike at the soma, which would in turn further expand the space of possible neuronal computations. In fact, new evidence from detailed computational modeling of V1 L2/3 pyramidal neurons indicates strong, sparse inputs to the dendrites dictate somatic responses (Goetz et al., 2021). Interestingly, although dendritic spikes in the apical tuft of L2/3 V1 pyramidal neurons may influence orientation selectivity (Smith et al., 2013), this orientation selectivity is robust to ablation of the apical tree (Park et al., 2019). Thus, in a realistic theory of visual processing, it is essential to scrutinize the functional effect that synaptic inputs along the basal and apical dendritic arbors have on the soma.

In this work, we used a detailed biophysical model of a L2/3 V1 pyramidal cell (Park et al., 2019), to tease apart the relative contributions of apical vs. basal dendritic trees in somatic orientation tuning. Given the evidence for sodium-dependent dendritic spikes in these neurons and their role in orientation tuning (Smith et al., 2013), the dendrites of these neurons, as well as their integrative properties, are clear targets for model experimentation seeking to illuminate orientation tuning at the somatic level.

We start by examining the properties of dendritic non-linearities, which are found to be varied along the apical and basal dendrites. By comparing the model to *in vivo* two-photon calcium fluorescence imaging data, we verified that dendritic and somatic spontaneous activity patterns in the model adequately reproduce experimental data.

We then simulate orientation tuning in our model and evaluate its responses to specific combinations of dendritic disparity and synaptic distribution, finding that the output of the model does not always match the expected orientation preference, instead deviating towards orientation preferences more closely matching either the apical or basal mean orientation preference.

We continue by evaluating the dependence of somatic spikes on dendritic voltage-gated sodium conductances (VGSCs) by performing just-in-time interventions that nullify the VGSCs on either the apical or basal tree prior to a somatic spike. This shows that the majority of stimulus-driven spiking activity is dependent on sodium spikes generated in the apical tree, revealing that apical and basal trees must contribute via different mechanisms to tuned somatic output. We investigated this further by examining the role of both specific ionic (VGSCs) and synaptic (AMPA/NMDA) mechanisms in shaping orientation tuning. Results indicate that apical VGSCs are critical for proper neuronal tuning, while basal VGSCs do not play a significant role. Conversely, AMPA and NMDA activity of both the apical and basal trees is necessary for orientation tuning at the level of the soma. A potential reason for this is that basal dendritic branches feature higher sodium spiking thresholds for similar electrotonic length constants compared to apical branches, reducing their propensity to generate sodium spikes compared to apical dendrites.

Our results provide evidence for a synergistic effect between the activity of the apical and basal trees, with apical and basal synaptically-driven depolarizations alongside apical sodium

spikes playing a critical role in somatic spiking. This synergy manifests in the form of temporally precise summation of apical and basal input, which together drive action potential generation in this neuronal type.

2. Methods

2.1. Model Description

The single neuron model was derived from the L2/3 V1 pyramidal cell model of (Park et al., 2019) created in the NEURON simulation environment (Hines & Carnevale, 2001). It is a morphologically detailed reconstruction, featuring 43 apical dendritic segments, 7 basal dendritic segments and an axon. As the model makes use of a variety of passive and active mechanisms (*Supplementary Tables 1-4*), its electrophysiological properties were validated against experimental data (Park et al., 2019). Neither the morphology nor the biophysical properties of the source model were altered, barring specific ion channel or synaptic mechanism conductance changes whenever specified.

The model features both excitatory and inhibitory synaptic input. Excitatory input was subdivided into background-driven (noise) and stimulus-driven, the latter consisting of orientation-tuned synapses. Inhibitory synapses are modeled as background-driven (inhibitory noise) which alongside background-driven excitatory synapses (excitatory noise) comprise the background-driven inputs. Stimulus-driven and background-driven synaptic input to the neuron is distributed uniformly on the target compartments using a density of 2 synapses per µm (DeFelipe & Fariñas, 1992; Schuz & Palm, 1989). Activation of synapses occurs via pseudo-randomly generated Poisson spike trains. Background-driven and stimulus-driven synapses feature different Poisson activation frequencies (0.11 Hz and 0.3 Hz,

respectively) to produce the electrophysiologically-recorded firing rates (Adesnik et al., 2012; Park et al., 2019).

We modulate the proportion of stimulus-driven excitatory synapses on the apical versus the basal tree in various experiments in order to examine the effects of synaptic input distribution on somatic output. In all cases, the amount of inhibition at the soma is 7% of the total inhibitory synapses (Defelipe et al., 2002). The default synapse distribution was 40% apical to 60% basal ("biologically plausible model"), in adherence with experimental data (excitation: 40% apical, 60% basal; inhibition: 33% apical, 60% basal, 7% soma) (Defelipe et al., 2002). The "inverse biologically plausible" model, conversely, features a 60% apical to 40% basal distribution (excitation: 60% apical, 40% basal; inhibition: 55.8% apical, 37.2% basal, 7% soma). The "even" model features a balanced distribution of synaptic input across both trees (even: excitation: 50% apical, 50% basal; inhibition: 46.5% apical, 46.5% basal, 7% soma). The synaptic distribution of the "even" and "inverse biologically relevant" models are not derived by experimental data, yet they allow for the investigation of apical and basal tree interactions under conditions of balanced or imbalanced synaptic input. We also make use of other distributions biased in either the apical or basal direction (referring to stimulus-driven excitatory input; from 10% basal – 90% apical to 90% basal – 10% apical, in steps of 10%). Similar to above, background-driven synapses closely follow the stimulus-driven synapse distribution in these cases, except for background inhibition, which always features 7% allocated to the soma.

For the results shown In *Supplementary Figure 5,* we kept the inhibitory and excitatory background inputs fixed at the levels of the "even" distribution, while exclusively varying the distribution of the stimulus-driven synapses (e.g. from 10% basal – 90% apical to 90% basal – 10% apical, in steps of 10%). This allows us to observe the impact of the full spectrum of

synaptic distributions on somatic output unobstructed by the effects of changes in the distribution of background inputs. For clarity, we note that the 60% basal – 40% apical condition of this set of simulations ("60:40" condition) is *not* the same as the "biologically plausible" model, as it features a different distribution of background inputs.

In our model, orientation preference was assigned on two levels: synaptic (input/single synapse) and dendritic (whole tree). Single synapse orientation preference is modeled as a synaptic weight vector biased towards a predefined orientation, which factors into the activation function of orientation-tuned synapses (Chen et al., 2013). Each synapse is assigned an orientation preference, with values being 0° to 360° in steps of 10°. This distribution of orientation preferences to the stimulus-driven synapses at the dendritic tree level followed a Gaussian probability density function wrapped around the unit circle:

$$f(s) = \frac{1}{W\sqrt{2\pi}} \sum_{k=-1}^{1} e^{-\frac{(s-b+2\pi k)^2}{2W^2}}$$

where W is the standard deviation (30°; (Chen et al., 2013)), s is the synaptic orientation preference and b is the mean of the distribution (apical or basal tree mean orientation preference, ranging from 0° to 90° in steps of 10°). The parameter k controls the wrapping around the unit circle, and takes the values [-1, -0.5, 0, 0.5, 1]. As a result, the mean orientation preference of each dendritic tree is biased towards the chosen mean orientation preference. We evaluated somatic/neuronal orientation preference using the approach described in section 2.3.3.

171 **2.2. Biophysical Manipulations**

172 The following manipulations aimed to evaluate somatic output under different sets of
173 conditions:
174 (1) Sodium (channel) blockage: selectively nullify (set to zero) VGSCs (g_{Na}) in a designated
175 compartment (e.g. apical tree, specific basal dendritic segments, or soma).
176 (2) Synaptic modulation: selectively alter synaptic conductances (g_{AMPA}/g_{NMDA}) in a designated
177 compartment or dendritic tree.
178 (3) Input manipulation: selectively deactivate specific types of input (excitatory stimulus-
179 driven and background-driven).
180

181 **2.3. Simulation Protocols**

182 All simulations were performed on our High-Performance Computing Cluster (Rocks 7.0) with
183 624 cores and 3.328 TB of shared RAM under CentOS 7.4 OS (Papadopoulos et al., 2003),
184 through the NEURON simulation environment (Hines & Carnevale, 2001). Model neuron
185 output measurements were obtained at a sampling rate of 10 KHz (dt = 0.1 ms).
186 The following simulation protocols were implemented for validation and simulation purposes:
187 (1) Iterative paired-pulse protocol (I3P): Used for the evaluation of dendritic non-linearities.
188 Following synaptic silencing and g_{Na} nullification in the entire model neuron excluding the
189 dendritic segment under investigation, a number (1-200, with step 1) of evenly spaced
190 (uniformly distributed) excitatory synapses are synchronously activated (2 pulses at 50 Hz).
191 Voltage at the midpoint of each dendritic segment was recorded to evaluate dendritic non-
192 linear behavior caused by sodium and NMDA spikes.
193 (2) Stimulation protocol: the model is simulated for 2500 ms (2.5 s), with oriented stimulus

presentation onset at 500 ms (0.5 s), lasting until the end of the simulation (duration 2 s).

(3) Orientation tuning validation protocol: Using the above stimulation protocol, we simulate 10 model "neurons" that feature different synaptic location patterns, defining 10 distinct *neuron IDs*. For each one of these neuron IDs, we use 10 different permutations, with different instances of the input spike trains, resulting in 10 different *simulation IDs* for each neuron ID. Stimuli of 18 different orientations (0° to 170° in steps of 10°) are then presented in separate simulations. The tuning curve is extrapolated by averaging firing rates across simulation IDs for each neuron ID. The overall tuning properties (width, OSI) were then computed through averaging responses across neuron IDs for each stimulus orientation. Neuron IDs with an OSI of less than 0.2 or a tuning width greater than 80° (as determined by a Gaussian fit) are excluded. If more than 20% of neuron IDs do not meet this criterion, the specific parameter combination is considered to not result in orientation tuning. No neurons were excluded based on the preceding criteria in our simulations.

(4) Orientation disparity protocol: To evaluate the contribution of the apical and basal trees in the somatic orientation preference, we keep the mean apical tree orientation preference fixed at 0°, and set the mean basal tree orientation preference to any one of 10 different values (0° to 90° in steps of 10°) (see also section 2.1). Thus, we introduce orientation tuning *disparity* between the two trees, ranging from 0° to 90°. Akin to the orientation tuning protocol, we independently generate 10 different neuron IDs with 10 different simulation IDs for each one and present stimuli as above (section 2.3.3). Orientation preference is then calculated as described above (section 2.3.3). If more than 20% of the neuron IDs are rejected (OSI < 0.2 or tuning width > 80°) for a given degree of orientation tuning disparity, then the model as a whole is deemed to exhibit no orientation tuning for that level of disparity.

In order to determine whether the somatic response follows the mean apical or basal tree

preferred orientation most closely, we compute the *expected* orientation preference of each neuron ID; that is, the orientation preference assuming a linear summation of the synaptic inputs. Specifically, we record the assigned orientation preference of all synapses per neuron ID, and then we use Euler's Formula to calculate the expected orientation preference for this neuron ID:

$$E_d = arctan\left(\frac{\sum_i sin(T_i^A) + \sum_j sin(T_j^B)}{\sum_i cos(T_i^A) + \sum_j cos(T_j^B)}\right)$$

Where E_d is the expected orientation preference for a degree of disparity d, i and j are the numbers of stimulus-driven apical and basal synapses respectively, and T^A and T^B are lists of synaptic orientation preferences for the apical and basal trees, respectively.

In this particular protocol, a remapping of preferences is required in specific cases (e.g. 180° → 0°), since we are not simulating direction selectivity, projecting orientation preferences into the [-90°, 90°) interval.

(5) <u>Spontaneous activity protocol:</u> Similarly to the orientation tuning validation protocol, we use 50 different neuron IDs with 100 different simulation IDs for each one. Simulations feature no stimulus-driven synaptic activity, leaving only background-driven synapses active.

(6) <u>Ionic intervention protocol</u>: Using 50 neuron IDs with 10 different simulation IDs for each one, prior knowledge of action potential occurrence is obtained via the stimulation protocol (see section 2.3.2; presented stimulus: 0°, corresponding also to the mean apical and basal tree orientation preference), using the 'biological plausible' synaptic distribution (section 2.1). This protocol proceeds similarly to the stimulation protocol (with the notable exception of somatic g_{Na} being set to 0 to prevent backpropagation) until a time before point t_i, which is the time of somatic spike occurrence. At t_i – 3 ms, g_{Na} is set to 0 on either the apical or basal

241 tree dendrites in two separate simulations, until t_i + 1 ms. This manipulation selectively
242 eliminates the contribution of apical or basal dendritic sodium conductances (seen either as
243 depolarization or as dendritic spikes) to the somatic spike. This protocol is repeated for all
244 somatic spikes and the ensuing voltage traces are analyzed to ascertain whether the somatic
245 spikes survived the manipulation. Spikes rendered extinct only when intervening on the apical
246 tree are labeled as "apically-driven", while those rendered extinct when intervening on the
247 basal tree are labeled as "basally-driven". The spikes rendered extinct by either intervention
248 are labeled as "cooperative". We observed no cases of somatic spikes failing to become
249 extinct in at least one of the two interventions while using this protocol.
250 (7) Synaptic intervention protocol: This protocol proceeds similarly to the ionic intervention
251 protocol (note that somatic g_{Na} is not set to 0 in this protocol), with two main differences: (a)
252 the intervention reduces stim-driven AMPA and NMDA synapse conductances on either the
253 apical or basal tree by a specific percentage (e.g. 50%, 90% etc.), rather than setting g_{Na} to 0,
254 (b) the window of the intervention changes from [t_i – 3 ms until t_i + 1 ms] to [t_i – 30 ms until
255 t_i +10 ms] (10x increase in window size). This was done to compensate for the relatively low
256 activation frequencies of stim-driven synapses (0.3 Hz).
257
258 **2.4 Two-Photon Microscopy**

259 (1) Animals in Experiments: All experimental protocols were approved by Brigham and
260 Women's Hospital (BWH) Institution Animal Care and Use Committee. Male and female wild-
261 type (C57BL/6) mice were purchased from The Jackson Laboratory and bred for experiments.
262 A total of 2 mice were used in these experiments.
263 (2) Chronic Window Implantation and Sparse Labeling: Viral vectors were purchased from

264 Addgene. For viral injections and chronic window implantation, 6-10 week old wild type
265 C57BL/6 mice (both male and female) were anesthetized with isoflurane (1-1.5%). The depth
266 of anesthesia was assessed via monitoring breathing rates. Meloxicam (2.5mg/kg) and
267 Buprenorphine (0.1mg/kg) were administered subcutaneously every 12 hours following the
268 surgical procedure for 2 days. A headpost was implanted on the skull and a 3mm diameter
269 craniotomy was made over the visual cortex of the left hemisphere. The craniotomy was
270 centered 2.7mm lateral to the midline and 1.5mm posterior to the bregma. To sparsely label
271 pyramidal neurons with GCaMP6s, a mix (~90 nl per site, up to 2 sites) of diluted CamKII-CRE
272 (AAV1, diluted 80,000X) and flex-GCaMP6s (AAV5, diluted up to 2X) was injected slowly over
273 5 minutes per penetration using a Drummond Nanoject III. Up to two penetrations ~0.5mm
274 apart on average were performed per craniotomy. After the viral injection, a round coverslip
275 was fitted to the craniotomy and sealed with vetbond and dental cement. Most chronic
276 windows in our hands remain clear for 2-3 months. 2-photon imaging was performed on week
277 3-4 following viral injection, at which time GCaMP6s expression was optimal.
278 (3) <u>In vivo calcium imaging of sparsely labeled neurons:</u> Three to four weeks after the
279 injection, each GCaMP6s expressing mouse was sedated with Fentanyl (0.5 mg kg^{-1}) and
280 Dexmedetomidine (0.5 mg kg^{-1}) (Mrsic-Flogel et al., 2007) for imaging experiments. A stable
281 level of anesthesia was confirmed by stable breathing rate and lack of movement. Neuronal
282 and dendritic calcium activity was recorded from L2/3 pyramidal neurons in V1. We chose
283 neurons with 1 to 3 primary basal dendritic segments clearly visible up to their primary
284 branching point on the same plane with the soma. Apical dendrites were not present in the
285 focal plane during recording. Mice were in the dark during the imaging process and their
286 spontaneous firing rate was recorded. Images were acquired at ~7.3 frames/sec using an
287 Ultima IV microscope in spiral scanning mode with a 25X 1.0 NA Nikon objective (5-30mW

288 laser power, 900 nm). Recordings lasted for 283 s (2750 frames). The size of the recording
289 FoV was 103 μm^2, and the pixel size was 0.201 μm^2. 12 pyramidal neurons were imaged, and
290 11 of these were selected for analysis. The final neuron was not selected due to an insufficient
291 number of basal dendritic segments being positively identified as belonging to said neuron
292 following visual inspection of a z-stack image.
293
294 **2.5. Data Analysis**

295 Data analysis of both modeling and two-photon imaging experiments was performed through
296 Python 3.8+, using publicly available libraries as well as custom-made scripts and functions.
297 The latter include:
298 (1) Dendritic Spike Detection: Dendritic sodium spikes were identified via a detection
299 algorithm that identified depolarizations exceeding a -20 mV threshold. For the identification
300 of NMDA spikes in the I3P experiments (see section 2.3.1) we located the inflection points
301 (points where the second derivative is zero) of the voltage trace after the second pulse. As
302 the NMDA spike exhibits a voltage plateau, 2 or more inflection points indicate an NMDA
303 spike. As our voltage measurements are not continuous and the I3P protocol does not feature
304 noise, it is unlikely to encounter a measurement point at which the second derivative is
305 exactly zero. Thus, we assume an inflection point exists at some recording point P_n if and only
306 if $(P_{n-1} \cdot P_{n+1}) < 0$, where P_{n-1} and P_{n+1} refer to existing points in the second derivative of the
307 voltage trace, immediately preceding and following the theorized inflection point.
308 (2) Quantification of Dendritic Nonlinearities: Using data from the I3P experiments, we
309 calculated the maximum amplitude of dendritic segment depolarization per synapse count. A
310 linear input-output curve is then generated, extrapolating from the response of the dendritic

311 segment to a single synaptic input (unitary response). This curve is compared to the actual
312 response of the dendritic segment to increasing input in an “Expected vs. Actual” plot, thus
313 coarsely characterizing the integration mode of the dendritic segment. The integration mode
314 of the dendritic segments was quantified in detail using the Nonlinearity Relative to Linear
315 Extrapolation (NRLE) metric (Behabadi et al., 2012), which is defined as the maximum ratio of
316 actual to expected neuronal output signal. An NRLE value of less than 1 denotes a sub-linear
317 dendritic segment, NRLE of exactly 1 indicates a linear dendritic segment and NRLE values
318 over 1 characterize a dendritic segment as supra-linear. The non-linearity threshold of all
319 dendritic segments was also calculated, measured as the minimum number of synapses
320 required to elicit the corresponding electrogenic event (sodium or NMDA dendritic spike).
321 (3) Two-Photon Imaging Data Analysis: Recordings are motion corrected via the suite2p
322 software (Pachitariu et al., 2016) to accurately extract fluorescence values from dendritic
323 segments. In the case of somatic activity data, we use the original video, as motion correction
324 is not necessary at the level of magnification used. Using the Fiji ImageJ software (Schindelin
325 et al., 2012), ROIs are manually defined, using a maximum intensity z-stack as a reference
326 image. Dendritic segments are identified as belonging to the cell of interest via visual
327 inspection of a z-stack recording. Each dendritic segment is broken up into multiple ROIs. Only
328 one ROI is defined for the soma. We completely avoid areas where there is an overlap of the
329 cell of interest with nearby dendrites/axons of cells from outside the field of view. Dendritic
330 ROIs are slightly wider than the dendritic segments themselves, to partially account for
331 misplacement of the ROI or uncorrected movement (drift) of the dendrite. 4 equal-sized
332 circular ROIs are also defined in areas where no visible dendritic segments or somata can be
333 found to calculate the background fluorescence level.
334 (4) Calcium Trace Processing: Raw calcium fluorescence data is normalized via a moving

335 window average of the fluorescence trace (window size of 20 s), subtracting F_0 from it
336 (defined as the average of the 20% lowest fluorescence values of said moving 20s window),
337 then dividing by the same value (F0), finally producing a normalized $\Delta F/F_0$ value. These $\Delta F/F_0$
338 values were significantly different from the background $\Delta F/F_0$ as calculated from the 4 circular
339 reference ROIs (cross-correlation test; $p < 0.05$; no manually-defined ROIs were excluded
340 through this process).
341 (5) <u>Calcium Event Detection:</u> Calcium events are detected via a simple dual-threshold
342 approach: a calcium event is registered when the ΔF/F value exceeds the 93.5^{th} percentile at
343 the same time as the derivative of the ΔF/F value exceeds the 67th percentile. These percentile
344 values were calculated via trial-and-error, attempting to match the expected firing frequency
345 of a neuron (soma) under spontaneous activity conditions (approximately 0.2 Hz (Haider et
346 al., 2013)). To ensure that the algorithm returns true events rather than random noise, we
347 performed an Event-Triggered Average (ETA) analysis. We extracted all of the detected event
348 waveforms, centered them on the time of detection, and averaged across waveforms. We did
349 this separately for somatic and dendritic events (*Figure 2C)*, as well as for each animal
350 separately (*Supplementary Figures 4A, 4B*). Calcium event-triggered averaging of the
351 processed fluorescence signal yields the expected temporal profile, indicating that these
352 events are not likely to represent noise.
353 (6) <u>Generation of "fluorescence-like" traces from model voltage traces:</u> 50 neuron IDs were
354 simulated with 100 simulation IDs each, using the "biologically plausible" configuration under
355 the spontaneous activity protocol, in order to closely match the properties of the real neurons
356 under spontaneous activity conditions. Next, we ran a spike detection algorithm to find all
357 somatic and dendritic spiking events. We binarized the traces, using 1 for spike peaks and 0
358 for everything else. We then convolved these binarized traces with a GcaMP6s kernel function

of our own design:

$$F(t) = -s\left(e^{-\frac{t-t_0}{t_r}} - e^{-\frac{t-t_0}{t_d}}\right)$$

Where t is time (in ms), s is a scaling factor (s ≈ 0.5714), t0 is the time of the event, t_r is the rise time (t_r = 74 ms) and t_d is the decay time (t_d ≈ 401.45 ms). The output of the function is unitless, representing fluorescence. With these parameters, our kernel function has an actual rise time constant of 194.225 ms, with output values decaying by ~52.11% within 0.6 s (*Supplementary Figure 2A*). These values closely match experimentally observed values for GCaMP6s (Chen et al., 2013) (*Supplementary Figure 2B*). The ensuing fluorescence traces were then downsampled to a dt of 0.138 s (~7.25 Hz) from the original dt of 0.1 ms (10 KHz), to emulate the sampling rate of two-photon calcium fluorescence imaging. The transformed traces were then processed by the same pipeline as true calcium fluorescence data (see points 4 and 5 above).

(7) <u>Electrotonic length constant calculation:</u> The electrotonic length constants (mentioned also in text as "electrotonic constants") of all dendritic segments were calculated using the formula from van Elburg & van Ooyen (2010):

$$\lambda_i = \sqrt{\frac{b_i r_m}{2r_a}}$$

Where i refers to the dendritic segment, λ_i is the electrotonic length constant, b_i is the radius of the branch, r_m is the specific membrane resistance and r_a is the intracellular resistivity.

382 **3. Results**

383 **3.1. Varied Dendritic Non-Linearities in the Model Neuron**

384 To ensure the validity of our modeling approach, we first examined dendritic integration by
385 characterizing the sodium spike properties of all dendritic segments separately (*Figure 1A*),
386 wherein a specific number of synapses is synchronously activated by two pulses at 50 Hz while
387 all other compartments are modeled as passive (I3P; see *Methods* 2.3.1), and the response of
388 each dendritic segment is assessed. Results show that the model can produce realistic
389 dendritic spikes (*Supplementary Figures 1C, D*), while the properties of the spiking events vary
390 between dendritic segments (*Figures 1B, C, D, Supplementary Figures 1A, B*). Both apical and
391 basal dendritic segments exhibit a large degree of variation in their spiking thresholds (*Figures*
392 *1E, F;* threshold synapse count mean and standard deviations: basal 12.286±6.649 sodium,
393 51.429±13.179 NMDA; apical 14.442±13.825 sodium, 40.721±23.675 NMDA). Dendritic
394 segments with high sodium spiking thresholds also tended to exhibit higher NMDA spiking
395 thresholds. To quantitatively characterize the nonlinear behavior of each dendritic segment
396 we used the Nonlinearity Relative to Linear Extrapolation (NRLE) metric (Behabadi et al.,
397 2012), which is an estimate of the degree of non-linear dendritic integration within a specific
398 branch (see *Methods,* section 2.5.2). Results indicate that all dendritic segments of the model
399 neuron exhibit non-linear input-output relations (*Figure 1D,* NRLE=1 denotes linear, NRLE<1
400 sublinear, and NRLE>1 supra-linear), in line with experimental observations (Smith et al.,
401 2013; Wilson et al., 2016). In addition, the NRLE values are relatively widely dispersed (values
402 ranging from >1 to ~3.5), providing a large dynamic range of possible dendrite-level
403 computations. The above results show that there is diversity in apical and basal dendritic
404 integration that can be exploited to modulate orientation tuning. These differences are

405 potentially, at least in part, the result of differences in the morphological and
406 electrophysiological features of these dendritic segments, as we found that sodium spiking
407 propensity seems to be correlated with the electrotonic length constant for each dendritic
408 segment (*Figure 6C*).

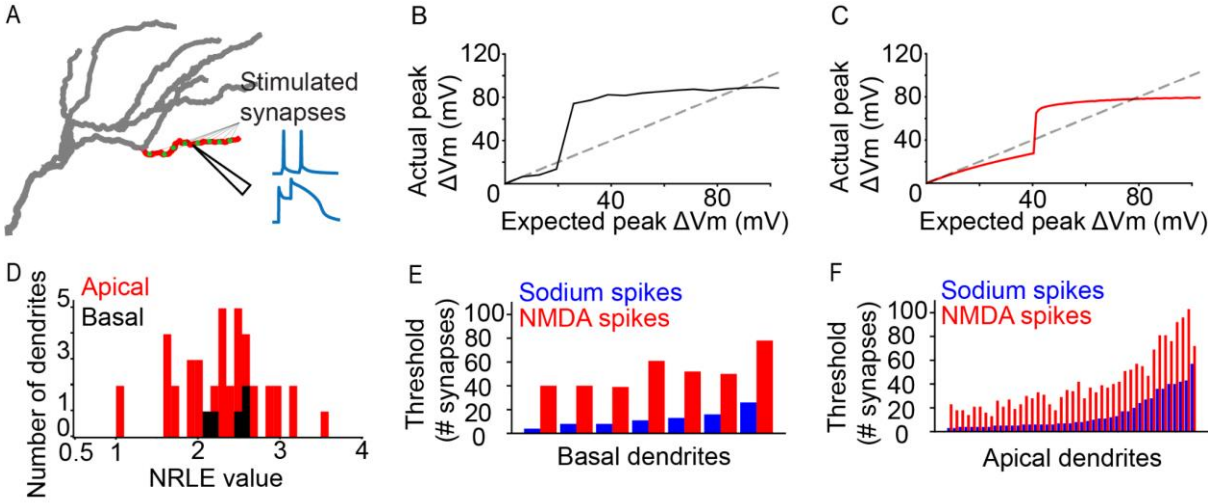

409

410 ***Figure 1. Dendritic Properties of a L2/3 V1 Neuron Model***. *A. Graphical representation of the iterative paired-*
411 *pulse protocol. Green dots represent allocated synapses. Synapses were activated only within the designated*
412 *(red) dendritic segment, with all other segments being passive. We record the voltage response of the dendritic*
413 *segment with NMDA channels disabled or enabled, acquiring information on dendritic sodium and NMDA spikes,*
414 *respectively. B. Example of an "expected vs. actual plot", showing the response (blue) of a single basal dendritic*
415 *segment to 1 to 200 simultaneous synaptic inputs compared to a linear (red). C. Same as B, but for an apical*
416 *dendritic segment. D. NRLE value histogram for all apical (red) and basal (black) dendritic segments. E. Bar plot*
417 *of per-dendrite nonlinearity thresholds for all basal dendritic segments, sorted by the sodium spike thresholds.*
418 *Note that NMDA spike thresholds partially follow the sodium spike threshold increase. F. As E, for all apical*
419 *dendritic segments.*

420

421 **3.2. Model Neuron Matches *in vivo* Spontaneous Activity Patterns**

422 Having validated the non-linear behavior of each dendritic segment, we now need to
423 adequately assess background-driven activity in our model. To assess this, we compare L2/3

424 V1 pyramidal neurons that were either imaged *in vivo* using two-photon calcium fluorescence
425 imaging, or simulated in our computational model. Specifically, simultaneous recordings from
426 basal dendritic segments and somata of L2/3 V1 pyramidal neurons were performed in
427 anesthetized mice (spontaneous activity of 11 neurons from 2 mice, see *Methods*, section 2.5;
428 *Figure 2A*). These imaging data were compared to modeling data generated using the
429 spontaneous activity protocol, whereby simulations feature only background activity, i.e.
430 noise, in the absence of a visual stimulus (see *Methods*, section 2.3). The resulting voltage
431 traces from the soma and basal dendritic segments were converted into approximations of
432 two-photon fluorescence traces (*Figure 2B* and *Supplementary Figure 2*, see *Methods*, section
433 2.5.6 for details) to allow a direct comparison with our *in vivo* calcium imaging data that were
434 collected under similar conditions (*Figures 2A - F*).

435 Significant fluorescence increase "events" were identified for both datasets using a custom
436 detection algorithm (see *Methods,* section 2.5.5). To ensure that the algorithm detects true
437 events rather than noise in the two-photon signal, we performed an event-triggered
438 averaging (ETA) analysis of trace segments centered on the event onset timepoint (see
439 *Methods,* section 2.5.5; 1131 dendritic events, 96 somatic events across all 11 neurons and
440 their respective dendritic ROIs). The results of this analysis indicate that random noise is
441 unlikely to be the cause of the detected events, as there is a marked increase in fluorescence
442 intensity at the time of event onset for all detected events (*Figure 2D*, *Supplementary Figures*
443 *3, 4*) which persists over time.

444 Next, in order to infer the relationship between basal and somatic events, we looked at their
445 relative timing differences. Using dendritic events as the starting point, we paired each
446 dendritic event with the most temporally proximal somatic event, and computed the time

difference between the two for each event pair (measured in imaging frames, each lasting approximately 138 ms). Using the same approach, we measured the fraction of somatic-dendritic event pairs in our model and compared them to the *in vivo* data. Event pairs featuring a temporal distance of zero (occurring within the same frame) were excluded as they are most likely to represent backpropagating events (excluded event pairs: model: 219,291/245,717 event pairs, 89.25%; *in vivo*: 29,143/237,572 event pairs, 12.27%; difference attributed to a lack of noise-related fluctuations in the model data compared with the *in vivo* data). The resulting distributions (*Figures 2E, F*) show that in both the model and *in vivo* data local dendritic events can be generated independently of somatic events. Paired events separated by more than 4 recording frames (~552 ms) are highly unlikely to be the result of backpropagation, even when considering the slow kinetics of the calcium sensor. Moreover, the somatic events that are preceded by basal dendritic events are similar in proportion between datasets (Figures 2E, 2F red bins: 48.79% model, 48.12% actual when including all event pairs with a non-zero timing difference; 24.3% model, 27.8% actual when including only event pairs with an absolute timing difference >4 recording frames). This analysis indicates that a notable number of detected somatic events are *not* closely preceded by any detected basal dendritic events, suggesting that other events, perhaps arising in the apical tree or not visible basal dendritic segments, contribute to somatic activity in such cases. It is important to note that the analyses herein are inherently subject to the noisy nature of the recordings, the limitations of the slow kinetics of the calcium indicator, the low temporal resolution of the recording (frame time of ~138 ms), as well as the possibility of undetected events.

To mitigate the risk that the *in vivo* findings are the result of noise or random chance, we constructed a null distribution of timing differences for the *in vivo* data by independently

circularly shuffling the time-series data from the somatic and various dendritic segment ROIs 1000 times, and then re-computed the timing differences. We then compared the actual data with the null distribution data using the two-sample Kolmogorov-Smirnov (KS) test, finding that the two distributions of timing differences were significantly different (*Supplementary Figure* 4C; test statistic ~0.105, $p << 0.05$), whereas a similar analysis of completely randomly generated event timings would results in identical (not statistically different) distributions for event pair timing differences.

In conclusion, we evaluated whether the background-driven activity of the model adequately approximates the dendro-somatic firing patterns seen in *in vivo* two-photon recordings (*Figure 2A*) of spontaneous activity in mice (*Figure 2C*). Both model and *in vivo* data feature "decoupled" dendritic events (*Figures 2E, 2F*), whereby dendritic events occur far in advance of the most temporally proximal somatic event. These events are not likely to be the result of noise, as event-triggered averaging analysis yields a distinct waveform and temporal profile (*Figure 2D, Supplementary Figures 3, 4A, 4B*). In addition, comparing the null distribution with the true data using the KS test, we find that the two are different (*Supplementary Figure 4C*). Thus, we can conclude that the model adequately reproduces *in vivo* spontaneous activity patterns.

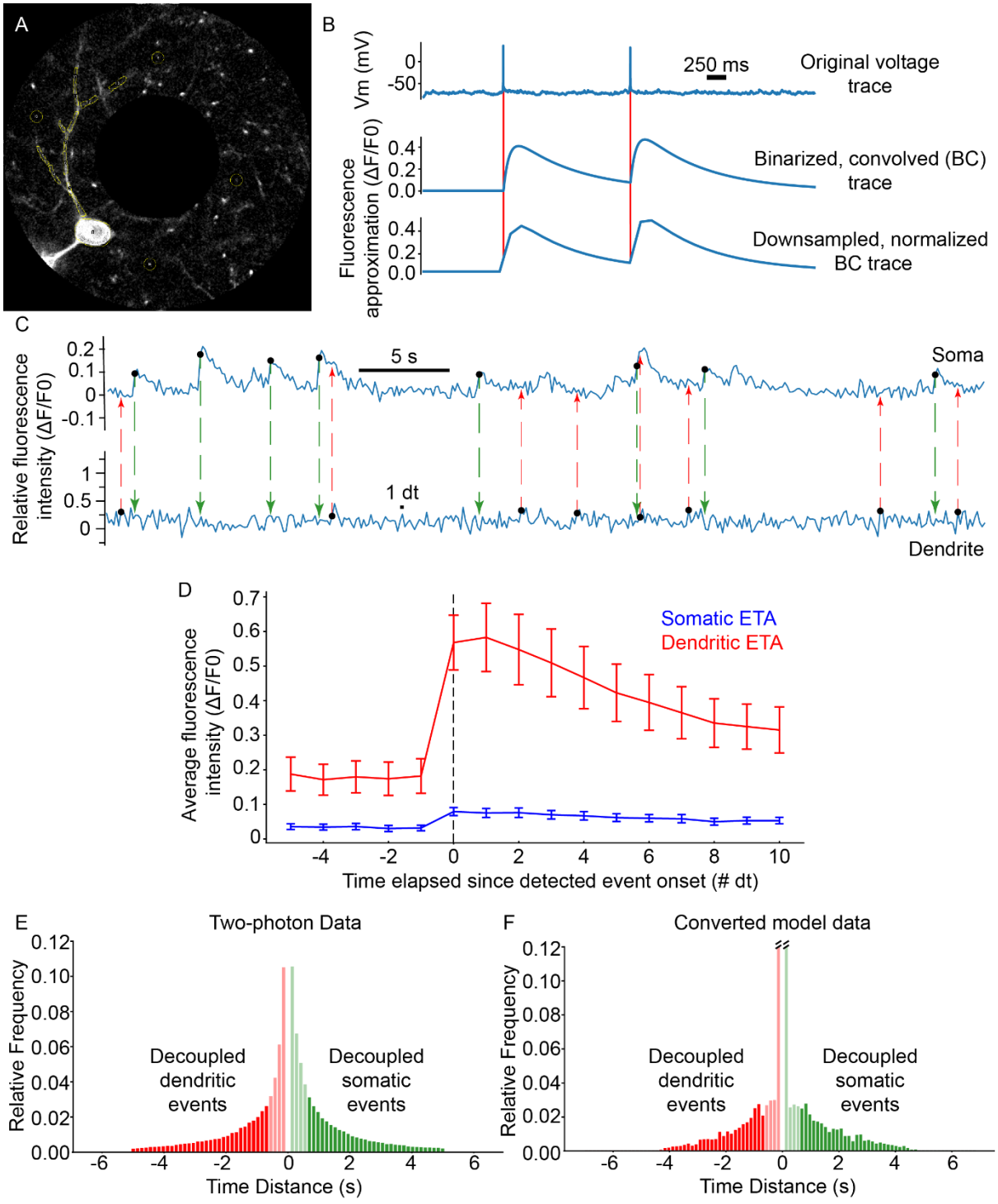

487

488 ***Figure 2. Comparing the Model Output with Two-Photon Imaging Data***. *A: Image from one of the neurons in*

489 *the dataset. Note the separate, multiple ROIs per dendritic segment, as well as the 4 circular ROIs used for*

490 *background fluorescence calculation. B: Example traces from the model data conversion pipeline. Voltage spiking*

491 *data is binarized and convolved with a GcaMP6s kernel function (*Supplementary Figure 2*). Resulting data is*

492 *downsampled to two-photon sampling rates (~7.25 Hz) from the original sampling rate (10 KHz), and processed*

exactly like in vivo *two-photon fluorescence data. Red vertical lines show the timing of the original spikes. C: Example somatic (top) and distal dendritic (bottom) $\Delta F/F_0$ traces from the neuron in (A). Black dots at the origin of colored dashed lines denote detected events. Note that somatic events (green dashed lines/arrows) are not necessarily coincident with dendritic events (red dashed lines/arrows). D: Event-triggered averages for all somatic (blue) and basal dendritic segment ROIs (1 dt $\simeq$ 0.138 s; error bars: Standard error of the mean). E: Event pair timing difference histogram for the two-photon data. 48.12% of event pairs feature basal dendritic events that are decoupled from the soma (red; dendritic events occur at least 1 dt before the onset of a somatic spike), with 27.8% being decoupled if the 4 bins (~552 ms) closest to zero are excluded (excluded data marked as lightly shaded bars). F: Event pair timing difference histogram for the converted model data. 48.79% of event pairs feature basal dendritic events that are decoupled from the soma (red; dendritic events occur at least 1 dt before the onset of a somatic spike), with 24.3% being decoupled if the 4 bins (~552 ms) closest to zero are excluded (excluded data marked as lightly shaded bars). Note that in both D and E, the zero-difference bin was removed, as it is assumed to contain the majority of backpropagating events. The middle two bars in F have been truncated for visualization purposes; the corresponding values are (left to right) 0.15958 and 0.16533, respectively.*

3.3. Model Neuron Features Robust Orientation Tuning

We have now shown that the model can accurately reproduce spontaneous activity patterns seen *in vivo*. The following experiments simulate stimulus-driven activity and orientation selectivity. To do so, we implement the orientation tuning validation protocol (*Figure 3C;* see *Methods,* section 2.3.3) for the biologically plausible model (see *Methods*, section 2.1), and derive the orientation tuning curve of the neuron (preferred orientation firing rate: 1.56±0.26 Hz, orthogonal orientation firing rate: 0.22±0.12 Hz, OSI 0.78±0.03, tuning width 43±1.45°; *Figure 3A*).

Next, we tried to disentangle the effects of the apical and basal trees by introducing dendritic disparity (*Figure 3B;* see *Methods,* section 2.3.4). To do so, we make use of the disparity protocol (see *Methods,* section 2.3.4; *Figure 3B*) in which the apical and basal trees are tuned

518 to different orientations: the apical tree features synaptic orientation preferences sampled
519 from a Gaussian distribution with a mean of 0°, whereas the basal tree uses the same method,
520 but with a different mean for its own distribution (0° - 90°, in steps of 10°). The expected
521 orientation preference of a neuron is calculated using Euler's Formula (see *Methods,* section
522 2.3.4).

523 We observe that under biologically plausible conditions, the model neuron appears to exhibit
524 a bias towards the preferred orientation of the basal tree – an example of *basal dominance*
525 (*Figure 3D*). Note also that the model did not exhibit adequate tuning beyond a dendritic
526 disparity of 40° (20% or more of neurons showed OSI<0.2 or tuning width >80°; see *Methods*,
527 2.3.3) To assess whether this is a feature of the model in general, or if it is the result of the
528 particular synaptic distribution used in the biologically plausible model, we repeated the
529 experiment using two different synaptic distribution profiles – the "inverse biologically
530 plausible" and "even" models (see *Methods,* section 2.1). We find that, indeed, the bias
531 displayed by the neuron appears to be decreased in the "even" model, and is clearly reversed
532 in the "inverse biologically plausible" model. Similar to the "biologically plausible" model,
533 these two models also did not feature adequate tuning past a certain dendritic disparity, 50°
534 in these cases. These results indicate that neuronal orientation preference is shaped, at least
535 in part, by the synaptic distribution along the two dendritic trees, as well as their mean
536 orientation preferences. In addition, orientation tuning persists up to a disparity of 40° in the
537 biologically plausible model, and up to 50° in the other models.

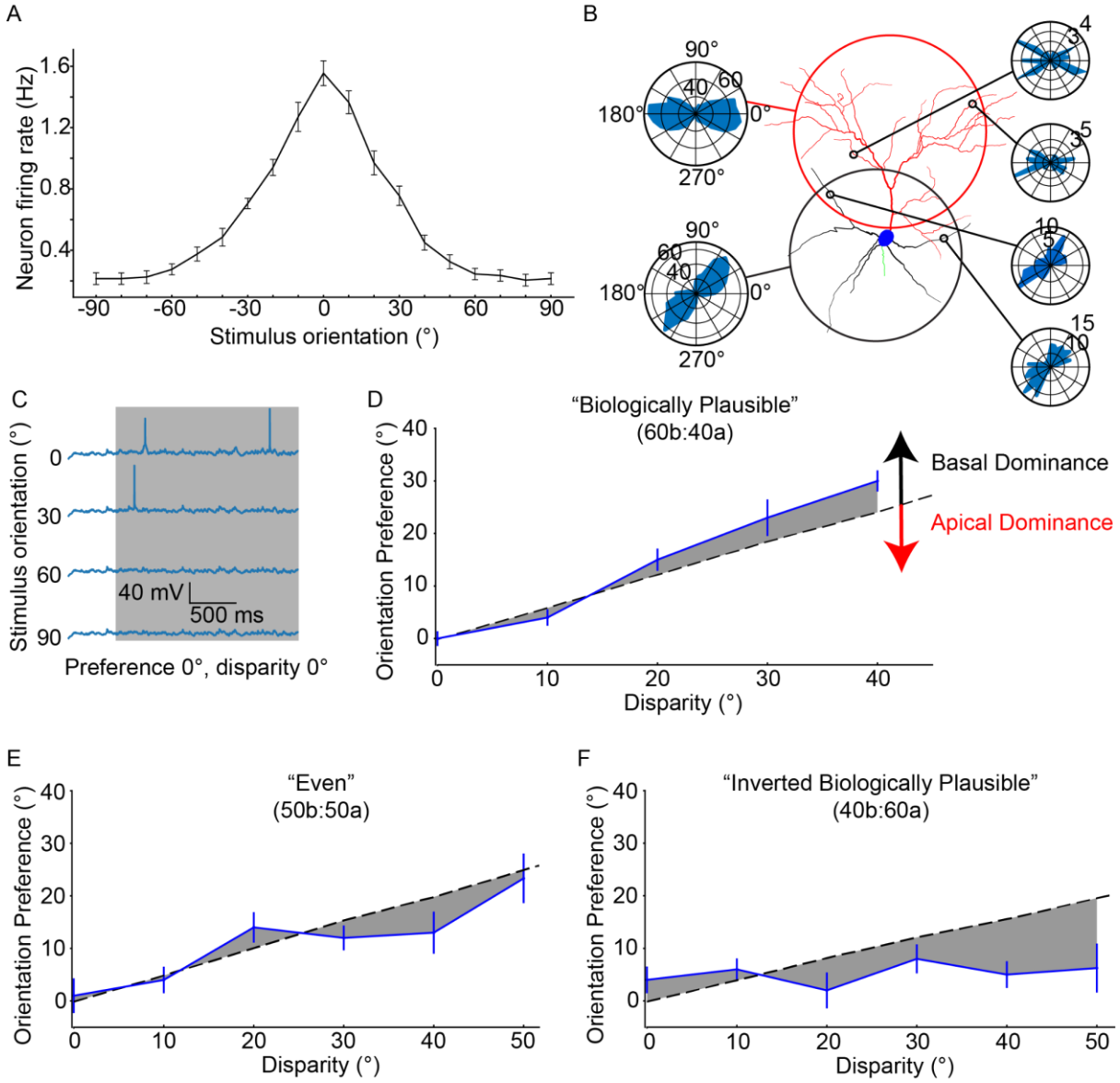

Figure 3. Neuronal Orientation Preference is Robust and Resists Dendritic Tuning Disparity*. A. Orientation tuning curve for the "biologically plausible" model. B: Example configuration of a model neuron set to a disparity of 40°. Right-side polar plots display the distribution of synaptic orientation preferences for the indicated dendritic segments. Left-side polar plots display the distribution of synaptic orientation preferences for the apical (top) and basal (bottom) dendritic trees. C: Example voltage traces recorded at the soma of a model neuron from (A). Note the clearly different responses between the preferred orientation (0°) and all others. D: Orientation preference plot for the "biologically plausible" model featuring various degrees of disparity. Grey dashed line denotes the expected orientation preference per degree of disparity. Black and red arrows point in the direction of basal and apical dominance, respectively. E: As D, but for the "even" model. Note that dominance has shifted from the basal domain towards the apical domain. F: As D, but for the "inverted biologically plausible" model.*

This configuration clearly features apical dominance. Error bars: Standard error of the mean, for all panels.

To fully characterize the effect of synaptic distribution on the contribution of each tree to neuronal tuning, we allocated different percentages (10%, 20% etc., up to 90%) of the total synapses (including all stimulus-driven, background-driven, excitatory and inhibitory) on a given tree (see *Methods,* sections 2.1 and 2.3.4), in a manner similar to how we generated the "inverse biologically plausible" model. As seen above (*Figure 3D, E, F*) somatic orientation preferences above the expectation curve produced by Euler's Formula indicate basal tree dominance, whereas those below the expectation line indicate apical tree dominance. We observe that the neuron does not always follow the expected orientation preference, indicating that the actual combined effect of apical and basal synaptic inputs is not linear. As such, apical and basal stim-driven inputs appear to cooperate in a non-linear fashion to produce somatic output.

3.4. Dendritic Sodium Spikes Alone are Insufficient to Explain Somatic Activity

The previous results show that orientation tuning is the result of the interaction between apical and basal trees, but were not enough to elucidate the exact contribution of each tree. In order to advance our understanding of the relative roles of each tree, we need to selectively intervene and interrupt specific aspects of their operation, judging their role by the effect of the intervention. The most obvious target for such an intervention is the sodium spiking activity of each dendritic tree, controlling for the type of input received (stimulus-driven vs background-driven). As such, we used the ionic intervention protocol (see *Methods* 2.3.6) in order to remove either the apical or basal sodium component of somatic activity.

We start by using the “biologically plausible” model with no alterations (“Control background”) and a preferred (0°) stimulus (case #1). In this condition, both stimulus-driven and background-driven synapses are active, and most synapses (60%; both stimulus-driven and background-driven) are allocated on the basal tree. We perform the intervention protocol for every recorded somatic spike under these conditions, and categorize these spikes in terms of dendritic sodium conductance dependence: “apically-driven” (dependent on the presence of apical sodium conductances), “basally-driven (dependent on the presence of basal sodium conductances) or “cooperative” (dependent on the presence of both apical and basal sodium conductances) (*Figure 5A*). We find that the majority of somatic spikes were dependent on apical sodium conductance (apically-driven 70.18%, basally-driven 12.28%, cooperative 17.54%; *Figure 5B)*, which is surprising, considering the proximity of the basal tree to the soma, as well as the nature and relevance of its feedforward inputs. These somatic events are both stimulus-driven and background-driven, so in order to separate the two, we change the orientation of the stimulus being presented to 90°, rendering the vast majority of stim-driven synapses inactive, while keeping background-driven synapses active as normal (case #2). We find that the percentages change drastically compared to the previous condition (apically-driven 33.33%, basally-driven 8.33%, cooperative 58.33%; *Figure 5D)*, indicating that the dependence of spiking activity on dendritic sodium conductance differs between cases of stimulus-driven and background-driven activity. In other words, the causality of spike generation differs between cases of stimulus-induced spiking versus spontaneous activity-induced spiking - at least in terms of their dependence on dendritic sodium conductances.

Importantly, however, we also need to eliminate the possibility of background-driven synapses being the main determinant of somatic spiking. Although background-driven

synapses feature low activation frequency (0.11 Hz vs 0.3 Hz for stimulus-driven), they are also vastly more numerous compared to stimulus-driven synapses (75% versus 25% of total synapses). To equalize the potential contribution of background-driven synapses to apical and basal tree output, we introduce a new condition ("Evenly distributed background") whereby the model is configured in the same manner as in case #1 (i.e. "biologically plausible" model), but we change the distribution of background-driven synapses to be the same on the apical and basal trees (i.e. excitatory: 50% apical, 50% basal; inhibitory: 46.5% apical, 46.5% basal, 7% soma). In this way, we ensure that the normally increased number of background-driven synapses on the basal tree is no longer a factor. Presenting a stimulus of the preferred orientation (0°) under these conditions (case #3), we find that the resulting percentages (apically-driven 85.53%, basally-driven 6.58%, cooperative 7.89%; *Figure 5C)* heavily resemble those seen in case #1, indicating that the change in background-driven synapse distribution did not substantially affect spike generation overall. By changing the orientation of the presented stimulus to 90°, we can evaluate whether the same holds for the background-driven spikes only (case #4). This does not appear to be the case, however, as the results (apically-driven 95.45%, basally-driven 4.55%, cooperative 0.00%; *Figure 5E)* do not resemble those seen in case #2. This implies that although spike generation overall is not substantially affected, the minority of spikes that are background-driven *are* affected, becoming reliant upon apical sodium conductances and completely losing their prior cooperatively-driven nature. One possible explanation for these results is that basal dendritic segments do not contribute significantly via sodium spikes, but also via AMPA- and NMDA-driven depolarizations - a possibility that we will explore further.

To further investigate how synaptic distribution impacts somatic spike dependence on

619 dendritic sodium conductance, we repeated the experiments above, but this time using a
620 variety of synaptic distribution profiles whereby the percentage of synapses on the basal tree
621 varies from 10% to 90% in steps of 10% (see *Methods,* section 2.1), with background-driven
622 synapses either following the stimulus-driven synapse distribution (control case) or being
623 evenly distributed (evenly distributed noise case). In the control case with a preferred
624 stimulus, we observe that as the basal tree receives more stimulus-driven synapses, the
625 dependence of somatic spikes on basal sodium conductance increases (*Supplementary Figure*
626 *5A*). In addition, the dependence of somatic spikes on apical sodium conductance never
627 reaches zero, even in the most extreme bias regime (*Supplementary Figure 5A*). Inversely, as
628 the apical tree receives more and more synapses, the dependence of somatic spikes on apical
629 sodium conductance increases, whereas the corresponding dependence on basal sodium
630 conductance actually reaches zero (*Supplementary Figure 5A*). A similar trend can be seen in
631 the control case using a non-preferred stimulus (*Supplementary Figure 5C*). Conversely, the
632 evenly distributed noise case does not feature any strong trends (*Supplementary Figure 5B*),
633 as the relative abundance of background-driven inputs overshadows the effect of the
634 relatively few stimulus-driven inputs (75% of excitatory input is background-driven, with the
635 remaining 25% being stimulus-driven (Chen et al., 2013; Park et al., 2019). Presentation of a
636 non-preferred stimulus results in identical results from all model configurations in this case,
637 as background-driven synapses are evenly distributed in all configurations, and the non-
638 preferred stimulus does not lead to activation of stim-driven synapses (*Supplementary Figure*
639 *5D*).
640

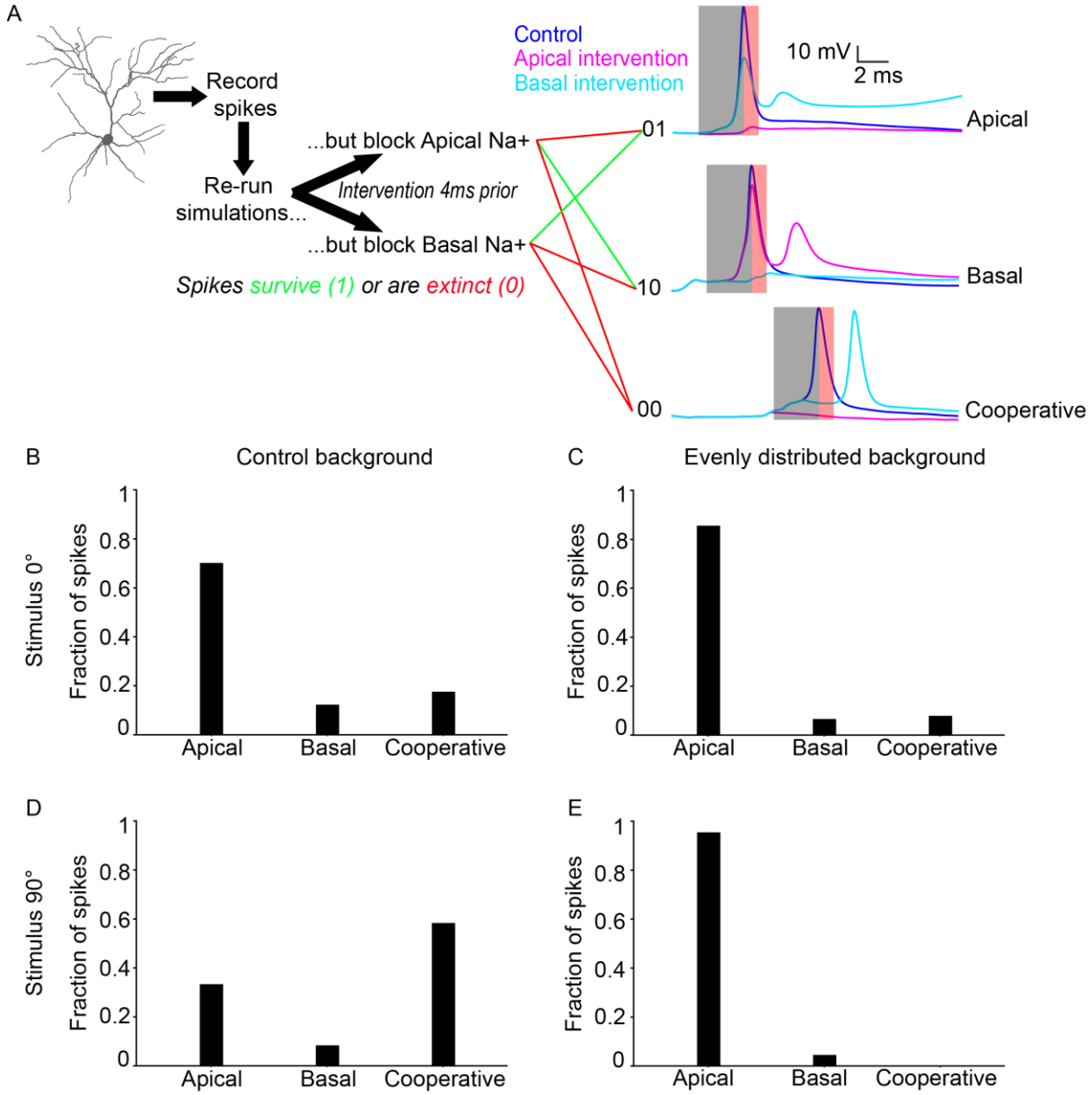

641

642 ***Figure 4. Neuronal Output Relies Disproportionately on Apical Sodium Conductance***. *A: Diagram describing the*
643 *ionic intervention protocol, with example traces on the right. Shaded areas on the traces denote the pre-spike*
644 *(grey) and post-spike (red) intervention time windows. B: Somatic spike dependence on dendritic sodium*
645 *conductance for the "biologically plausible" model with a stimulus of 0° (preferred orientation). C: Same as B, but*
646 *background synapses follow the "even" model (evenly distributed), while stimulus-driven synapses follow the*
647 *"biologically plausible" (60% basal, 40% apical) model. D: Somatic spike dependence on dendritic sodium*
648 *conductance for the "biologically plausible" model with a stimulus of 90° (orthogonal/non-preferred orientation).*
649 *E: Same as D, but background synapses follow the "even" model (evenly distributed), while stimulus-driven*
650 *synapses follow the "biologically plausible" (60% basal, 40% apical) model.*

3.5. Apical and Basal Dendrites Influence Somatic Tuning via Different Mechanisms

The previous results contain a counter-intuitive observation: although we would expect both apical and basal dendritic segments to contribute to somatic output, it appears that the contribution of the apical tree overshadows the basal tree significantly, at least as far as sodium conductance is concerned. Naturally, the basal tree, being the bearer of the majority of feedforward inputs, is very unlikely to have a minor role in the function of the neuron, and orientation tuning in particular. As such, it is reasonable to assume that it exerts its influence via a different mechanism. To assess the veracity of this assumption, we performed a series of experiments aimed at evaluating the impact of different ionic (see *Methods,* sections 2.2.1 and 2.3.6) and synaptic (see *Methods,* sections 2.2.2, 2.2.3 and 2.3.7) mechanisms on neuronal orientation tuning, using a stimulation protocol (see *Methods,* section 2.3.2) with the biologically plausible model.

First, we assess the tuning characteristics of the neuron when stimulus-driven input only is removed either from the apical (apical target) or from the basal tree (basal target) (see *Methods,* section 2.2.3), and compare it with the control case (in which both trees receive input as normal). We find that the neuron remains tuned in both cases, albeit with significantly decreased OSI values (t-test: control vs basal target: $p = 0.0002$; control vs apical target: $p = 0.008$) (*Figure 5A*).

Next, we use a synaptic intervention protocol to selectively reduce synaptic (AMPA and NMDA) weights by 50% on either the apical (apical target) or basal tree (basal target) for a brief time only, and only when a somatic spike is about to occur (see *Methods,* section 2.3.7), comparing with the control condition where no intervention takes place. Results show that tuning is completely abolished when basal AMPA and NMDA weights are reduced (*Figure 5B*),

whereas tuning persists, albeit significantly affected, in the apical intervention case (t-test; control vs apical target: $p \approx 0.00004$). We also perform a similar experiment, reducing AMPA and NMDA weights by 90% throughout the simulation for either the apical (apical target) or basal tree (basal target) (see *Methods,* section 2.2.2), and comparing with the control case. We find that the neuron remains tuned in these cases, albeit with significantly decreased OSI values (t-test: control vs basal target: $p = 0.0011$; control vs apical target: $p = 0.0168$) (*Supplementary Figure 6*). These results indicate that both apical and basal synaptic (AMPA and NMDA) activity is necessary for orientation tuning.

We then move on to assessing the impact of sodium conductance nullification on orientation tuning. We use an ionic intervention protocol to selectively nullify sodium conductance on either the apical (apical target) or basal tree (basal target) for a brief time only, and only when a somatic spike is about to occur (see *Methods,* section 2.3.6), again comparing with the control condition where no intervention takes place. We discover that precise loss of apical sodium conductances completely abolishes orientation tuning in the neuron (*Figure 5C*), but precise loss of basal sodium conductances does not affect orientation tuning (t-test; control vs basal target: $p = 0.3473$). The next experiment is similar, and less temporally precise – we completely nullify sodium conductance on either the apical (apical target) or basal tree (basal target) throughout the experiment, comparing with the control where no change in conductance has taken place (see *Methods,* section 2.2.1). Unsurprisingly, the results are nearly identical - total loss of apical sodium conductances completely abolishes orientation tuning in the neuron (*Supplementary Figure 6*), but total loss of basal sodium conductances does not affect orientation tuning (t-test; control vs basal target: $p = 0.6767$).

From these experiments we can surmise that apical sodium conductance is necessary for both

spike generation in general (*Figure 4, Supplementary Figure 5)* as well as for orientation tuning in particular (*Figure 5C, Supplementary Figure 6).* Conversely, AMPA and NMDA activity is necessary for both apical and basal trees (*Figures 5A, 5B, Supplementary Figure 6)*. This means that the apical tree most likely exerts its influence on somatic spiking via AMPA- and NMDA-driven sodium spikes, whereas the basal tree mostly utilizes AMPA- and NMDA-driven depolarizations, rather than sodium spikes.

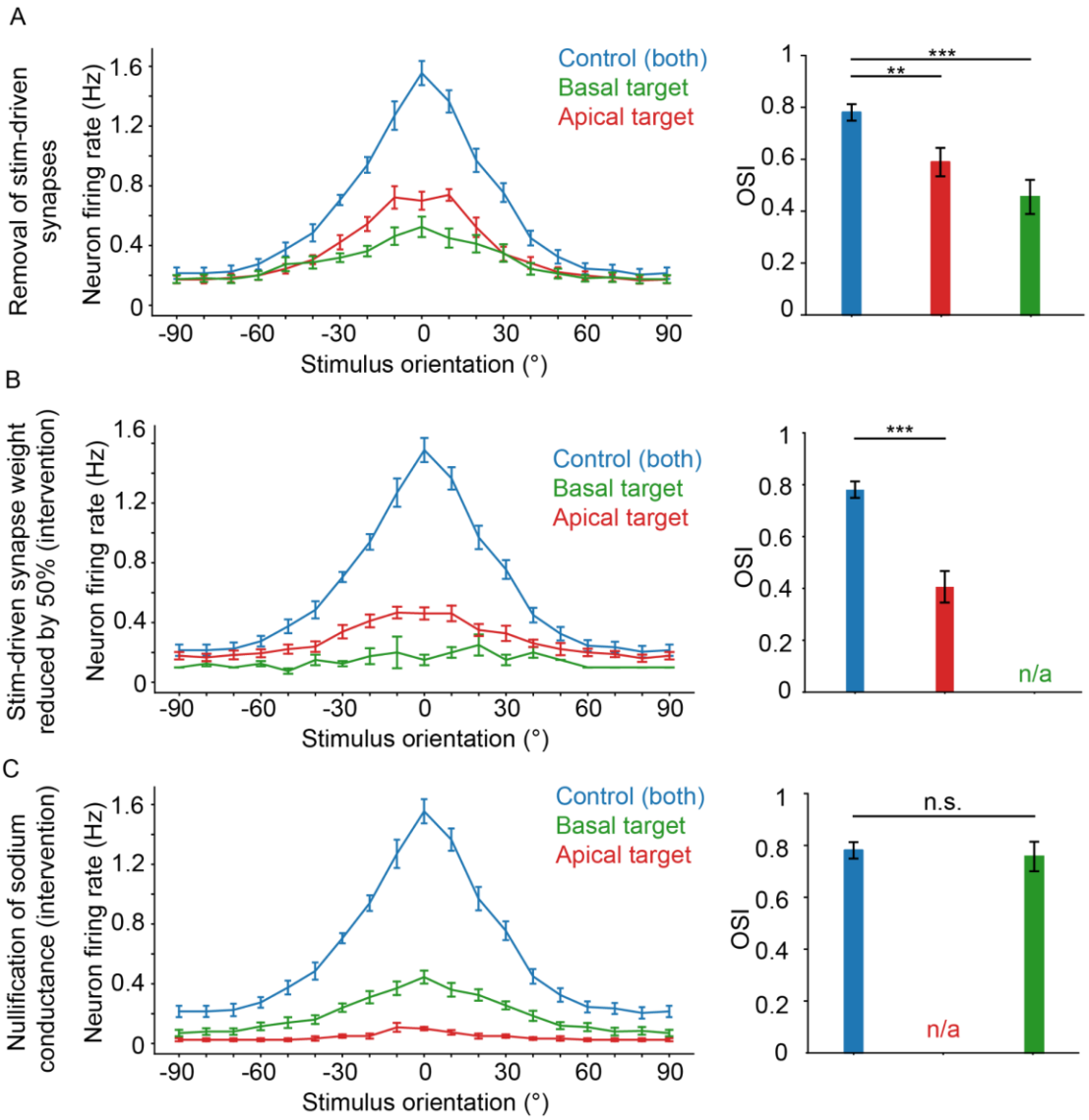

Figure 5. Orientation Tuning Critically Depends on Apical Sodium Conductance and AMPA/NMDA Activity. *A: Orientation tuning curves (left) and mean OSI values (right) for the experiment where stimulus-driven synapses*

706 *are completely absent on either the apical ("apical target"; red) or basal ("basal target"; green) tree. B: Selective*
707 *reduction of stim-driven synaptic (AMPA/NMDA) weights by 50% 30 ms prior to somatic spike occurrence (lasting*
708 *up to 10 ms after the pre-recorded somatic spike timing), on either the apical (apical target; red) or basal (basal*
709 *target; green) tree. C: Nullification of sodium conductances 3 ms prior to somatic spike occurrence (lasting up to*
710 *1 ms after the pre-recorded somatic spike timing), on either the apical (apical target; red) or basal (basal target;*
711 *green) tree. Error bars: Standard error of the mean, for all panels. "n/a" denotes a lack of orientation tuning for*
712 *that experimental setup. Stars denote statistical significance at a significance level (α) of 0.05 (*), 0.01 (**) or*
713 *0.001 (***), whereas "n.s." stands for "no statistically significant difference", i.e. p-value ≥ α.*
714

715 **3.6. Morphological and Electrophysiological Properties Influence Dendritic Behavior**

716 It is now clear that apical and basal dendritic segments exert causal influence on somatic spike
717 generation via separate mechanisms. In *Figure 1*, we showed the wide array of dendritic non-
718 linear behaviors present in the dendritic segments of the neuron. Here, we investigate the
719 relationship between the sodium spiking threshold of dendritic segments (henceforth
720 "threshold") and specific morphological and electrophysiological properties, attempting to
721 link the physiology of dendritic segments with their contribution to somatic spiking.

722 We first look into the diameter of dendritic segments, finding that there is a rough linear
723 relationship between diameter and threshold (*Figure 6A*). Outliers, marked as "atypical",
724 feature small diameters and very short lengths (lengths: 16.2±10.5 µm; diameters:
725 0.711±0.027 µm) but relatively high sodium spiking thresholds. Next, we look into distance
726 from the soma rather than diameter. Given the morphology of the neuron (see *Figure 6D* for
727 an illustration), basal dendritic segments are clearly much closer to the soma compared with
728 the majority of apical dendritic segments, located far from the soma, on the apical tuft. We
729 find that there is no clear relationship between distance and threshold (*Figure 6B*). The last
730 parameter we will look into is the electrotonic length constant (see *Methods,* section 2.5.7).

In order to avoid comparing basal dendritic segments with apical trunk or atypical dendritic segments that feature extremely high thresholds, we excluded all such dendritic segments, as well as any others matching their electrotonic length constant values, from further analysis (*Figure 6C*; trunk segments marked in teal, atypical dendritic segments marked in green, grey area denotes excluded dendritic segments). After excluding these dendritic segments, we performed a linear regression for the remaining apical and basal dendritic segments, generating one fit line for each (*Figure 6C;* basal dendritic segments: red dashed line, apical dendritic segments: black dashed line). Inspection of the regression fit lines reveals that basal dendritic segments feature higher sodium spiking thresholds than apical dendritic segments for the same electrotonic length constant values, offering a potential explanation for the large role apical sodium conductances play in shaping somatic output.

Finally, we can combine our observations of the contributions of apical and basal dendritic segments to the operation of the neuron. We predict that neuronal output in L2/3 V1 pyramidal cells depends on the timely interaction of appropriate apical and basal inputs to the soma (i.e. apical sodium spikes coinciding with basal depolarizations and/or spikes), a phenomenon we dub *Bilateral Input Coincidence (BIC)* (*Figure 6D*): rather than solely relying on inputs from one tree alone, L2/3 V1 neurons rely on the cooperation between apical and basal inputs to produce their orientation-tuned output.

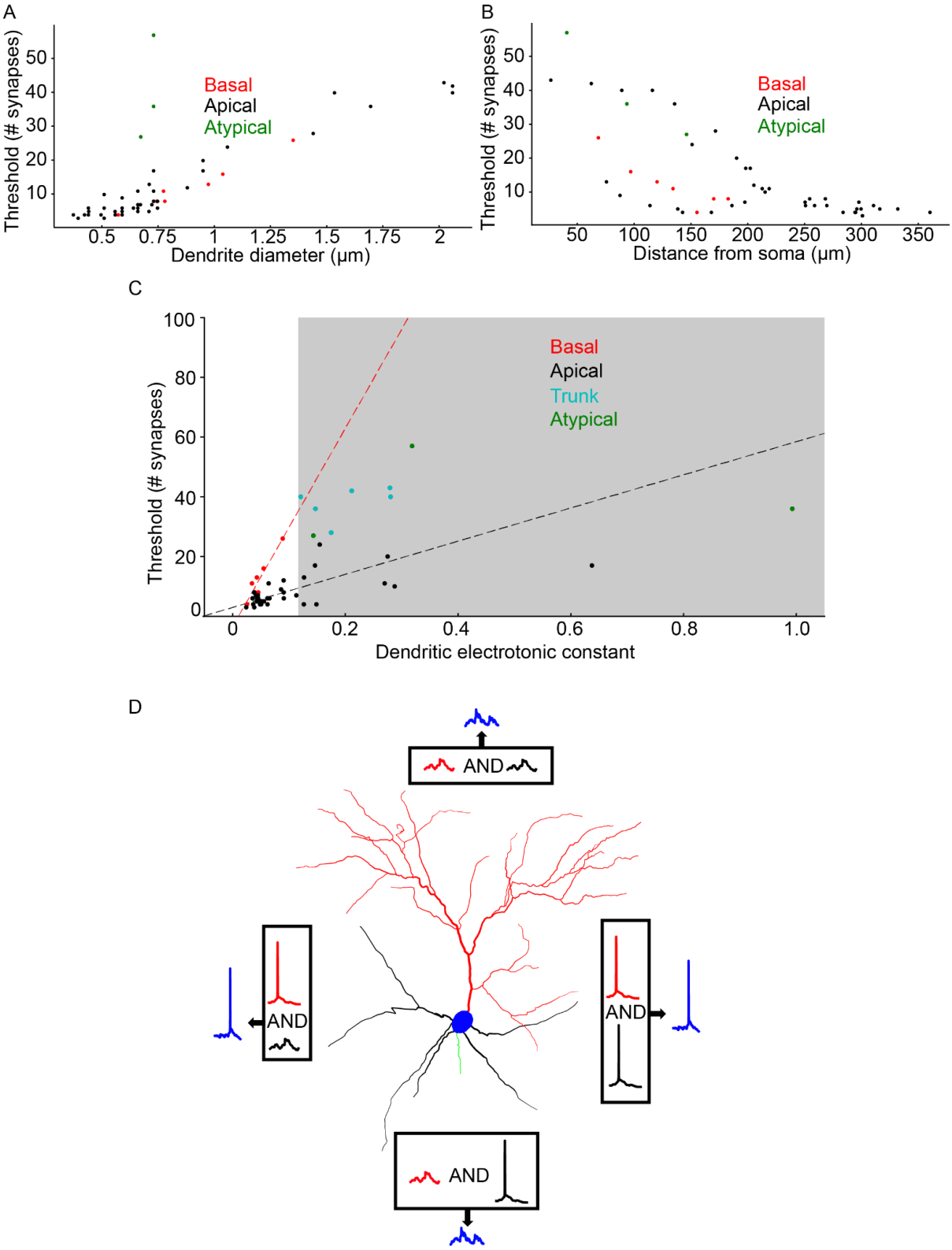

753

754 ***Figure 6. Neuronal Output as a Function of Physiologically Distinct Dendrite Outputs.*** *A: Sodium spiking*

755 *threshold for basal (black), apical (red) and atypical (morphological outliers, typically featuring unusually high*

756 *thresholds; green) dendritic segments as a function of their diameter. B: As A, but for dendritic segment distance*

757 *from the soma (measured from their midpoint) rather than diameter. C: As A, but for the electrotonic length*

constant rather than distance to the soma. Trunk segments (proximal and distal trunk) marked in teal. Red and black dashed lines indicate lines fit using linear regression for the basal (red) and apical (black) dendritic segments, respectively, excluding all dendritic segments within the area marked in grey. Note that for similar values of the electrotonic length constant, the basal dendritic segments feature a higher sodium spiking threshold. D: Schematic representation of Bilateral Input Coincidence (BIC). Somatic spiking is achieved when apical sodium spikes coincide with basal depolarizations and/or spikes. Basal spikes combined with apical depolarizations or depolarizations from both trees are generally unable to elicit somatic spiking.

4. Discussion

In this work, we have delineated the dendritic constituents of neuronal computation in L2/3 V1 pyramidal cells using a detailed computational model. We showed that the model exhibits a wide range of non-linear behavior on the dendritic segment level (*Figure 1*), and that it can accurately model the output of real neurons under spontaneous conditions (*Figure 2*). Inspecting the behavior of the neuron under conditions of tuning disparity, we find that it remains robustly tuned (OSI < 0.2 and tuning width > 80°) for non-extreme dendritic disparity conditions, although the exact orientation preference does not necessarily always match the expected one (*Figure 3*), indicating that apical and basal inputs exhibit non-linear cooperativity. This is seemingly contradicted by our following finding, where we show that the dependence of somatic sodium spikes on basal sodium conductances is low (*Figure 4*) under biologically plausible conditions, or even zero in other synaptic distribution regimes that heavily favor the apical tree (*Supplementary Figure 5*). The contradiction is resolved, however, by taking into account the subsequent finding that orientation tuning requires apical sodium channel conductances, but does not necessarily require basal sodium channel conductances (*Figure 5*). An explanation for this observation might be that basal dendritic

783 segments feature morphological and electrophysiological properties that endow them with
784 higher sodium spiking thresholds, which renders basal sodium channels much less effective
785 at eliciting somatic responses compared to those located on the apical tree (*Figure 6C*). On
786 the other hand, AMPA and NMDA conductances are necessary in both dendritic trees for
787 orientation tuning. This indicates that depolarizations from the basal tree play a key role in
788 shaping neuronal output, even when basal sodium spikes do not. As such, neuronal output
789 must be a synergistic phenomenon mostly between apically-based sodium spikes and basally-
790 based depolarizations or sodium spikes. Our results thus indicate that a form of *intra-tree*
791 *dendritic cooperativity* - a synergistic effect between apical and basal dendritic segments that
792 exhibit activity in relative synchrony - might be present in these neurons. This is evidenced by
793 the existence of extinction-prone "cooperative" somatic spikes that are lost when either of
794 their dendritic components (apical or basal, be that depolarization or spiking) is lost (*Figure*
795 *4*). Additional evidence is provided by the previously mentioned experiments in which
796 removing basal inputs altogether silences the neuron, despite plentiful apical tree activity, as
797 well as through experiments in which removal or suppression (weight reduction) of basal
798 stimulus-driven synapses (i.e. only background-driven synapses are fully active) significantly
799 decreases OSI values in the model neuron (*Figures 5A, 5B*).
800 Finally, driven by our observations we hypothesize that somatic output is determined through
801 *Bilateral Input Coincidence*, a subcategory of coincidence detection (*Figure 6D*). The basal tree
802 receives visual feedforward input, representing the information therein as a series of
803 hyperpolarizations, depolarizations, and occasional dendritic spikes. Thus, visual input creates
804 a basal "backdrop" of depolarizations that represents visual information. At the same time,
805 predictive and attentional signals from higher-order cortical areas reach the apical tree of the
806 neuron, causing the generation of dendritic spikes that propagate to the soma and are

temporally summed with any concurrent basal depolarization. In the event that visual input is non-existent, or of a non-preferred orientation, the depolarization is minimal to none. Thus, the apical dendritic spike will not be significantly augmented through summation and will fail to produce a somatic response in the majority of cases. If there is visual input, however, especially of an orientation matching the preferred orientation of the basal tree, the aforementioned “backdrop” will include multiple subthreshold depolarizations, perhaps even dendritic spikes. The apical dendritic spikes are thus likely to be temporally summed with these depolarizations and generate a somatic spike. As such, even though most somatic spikes will be generated through an apical tree dendritic spike, the cases in which this is possible in the first place will be dictated by the backdrop of depolarizations (and/or spikes) provided by the basal tree. On the face of it, this finding apparently contradicts the findings of Park et al. (2019), where *in vivo* micro-ablation via laser of the apical tree in L2/3 mouse V1 pyramidal neurons did not abolish orientation selectivity, which remained essentially unchanged following a recovery period of ~ 1 day. This apparent disparity can be potentially explained by postulating the operation of cellular homeostatic mechanisms that might alter the dependence of somatic spiking on basal inputs.

Our hypothesis also suggests that L2/3 V1 pyramidal cells may perform salient feature extraction from visual input compatible with predictive coding (Rao & Ballard, 1999). Our hypothesis suggests that when top-down signals reflecting attentional or predictive processes reach the apical tree, they “highlight” appropriate parts of the signal “landscape” generated by the visual input reaching the basal trees. This could result in a neuron that is activated only when specific features are present in its receptive field, facilitating the processing of salient stimuli. Such phenomena have been observed experimentally as a result of attention (Simons & Chabris, 1999).

However, multiple questions still remain unanswered. First of all, the exact nature of the attentional and predictive signals received by the apical tree remains to be deciphered. Secondly, the formation of the visual “backdrop” as a result of basal tree depolarization merits further study. Encoding of visual information using mostly subthreshold depolarizations in the presence of noise is an interesting problem, possibly resolved through the effects of intra-tree dendritic cooperativity, where apical spikes sharpen responses to stimulus-driven input rather than noise. In addition, a number of differences emerge when comparing the visual system across different model species. In rodents, orientation-selective cells akin to V1 simple cells have been discovered in the thalamus itself (Scholl et al., 2013), and direct thalamocortical projections to L1 of V1 have also been observed (Roth et al., 2016). In addition, rodent V1 organization follows a dispersed salt-and-pepper motif, unlike the highly structured organization typical of higher mammals like primates and cats (Ohki & Reid, 2007). These differences are important to take into account when trying to infer general rules of function from information derived from rules of information processing in different animal models. Finally, perhaps the most interesting unanswered question is whether these computations take place elsewhere in the cortex in addition to the visual system. Predictive coding as a means of stimulus compression has already been proposed as a way to simplify visual perception (Rao & Ballard, 1999), and this might also be the case for other sensory or cognitive tasks. Regardless, further investigation is required in order to unravel the Gordian knot that is visual perception.

5. Acknowledgments

This work was supported by the ERC Starting Grant "dEMORY: Dissecting the role of dendrites in memory", ERC-2012-StG-311435, the Fondation Santé, a FORTH-Synergy Grant (EVO-NMDA) and the NEUREKA grant H2020-FETOPEN-2018- 2019-2020-01 to YP, and the NIH NEI R01 grant EY-024019 and NINDS R21 grant NS088457 to SS.

6. References

1. Adesnik, H., Bruns, W., Taniguchi, H., Huang, Z. J., & Scanziani, M. (2012). A neural circuit for spatial summation in visual cortex. *Nature*, *490*(7419), 226–231. https://doi.org/10.1038/nature11526
2. Behabadi, B. F., Polsky, A., Jadi, M., Schiller, J., & Mel, B. W. (2012). Location-dependent excitatory synaptic interactions in pyramidal neuron dendrites. *PLoS Computational Biology*, *8*(7), 40–42. https://doi.org/10.1371/journal.pcbi.1002599
3. Chen, T.-W., Wardill, T. J., Sun, Y., Pulver, S. R., Renninger, S. L., Baohan, A., Schreiter, E. R., Kerr, R. A., Orger, M. B., Jayaraman, V., Looger, L. L., Svoboda, K., & Kim, D. S. (2013). Ultrasensitive fluorescent proteins for imaging neuronal activity. *Nature*, *499*(7458), 295–300. https://doi.org/10.1038/nature12354
4. Cho, K.-H., Jang, H.-J., Lee, E.-H., Yoon, S. H., Hahn, S. J., Jo, Y.-H., Kim, M.-S., & Rhie, D.-J. (2008). Differential Cholinergic Modulation of Ca2+ Transients Evoked by Backpropagating Action Potentials in Apical and Basal Dendrites of Cortical Pyramidal Neurons. *Journal of Neurophysiology*, *99*(6), 2833–2843. https://doi.org/10.1152/jn.00063.2008
5. Coogan, T. A., & Burkhalter, A. (1990). Conserved patterns of cortico-cortical connections define areal hierarchy in rat visual cortex. *Experimental Brain Research*, *80*(1), 49–53. https://doi.org/10.1007/BF00228846
6. Cruz-Martín, A., El-Danaf, R. N., Osakada, F., Sriram, B., Dhande, O. S., Nguyen, P. L., Callaway, E. M., Ghosh, A., & Huberman, A. D. (2014). A dedicated circuit links direction-selective retinal ganglion cells to the primary visual cortex. *Nature*, *507*(7492), 358–361. https://doi.org/10.1038/nature12989
7. Defelipe, J., Elston, G. N., Fujita, I., Fuster, J., Harrison, K. H., Hof, P. R., Kawaguchi, Y., Martin, K. A. C., Rockland, K. S., Thomson, A. M., Wang, S. S. H., White, E. L., & Yuste, R. (2002). Neocortical circuits: Evolutionary aspects and specificity versus non-specificity of synaptic connections. Remarks, main conclusions and general comments and discussion. *Journal of Neurocytology*, *31*(3-5 SPEC. ISS.), 387–416. https://doi.org/10.1023/A:1024142513991
8. DeFelipe, J., & Fariñas, I. (1992). The pyramidal neuron of the cerebral cortex: morphological and chemical characteristics of the synaptic inputs. *Prog Neurobiol*, *39*(6), 563–607. https://doi.org/10.1016/0301-0082(92)90015-7
9. Goetz, L., Roth, A., & Häusser, M. (2021). Active dendrites enable strong but sparse

inputs to determine orientation selectivity. *Proceedings of the National Academy of Sciences of the United States of America*, *118*(30). https://doi.org/10.1073/pnas.2017339118

10. Haider, B., Häusser, M., & Carandini, M. (2013). Inhibition dominates sensory responses in the awake cortex. *Nature*, *493*(7430), 97–100. https://doi.org/10.1038/nature11665
11. Hines, M. L., & Carnevale, N. T. (2001). Neuron: A Tool for Neuroscientists. *The Neuroscientist*, *7*(2), 123–135. https://doi.org/10.1177/107385840100700207
12. Iacaruso, M. F., Gasler, I. T., & Hofer, S. B. (2017). Synaptic organization of visual space in primary visual cortex. *Nature*. https://doi.org/10.1038/nature23019
13. Jia, H., Rochefort, N. L., Chen, X., & Konnerth, A. (2010). Dendritic organization of sensory input to cortical neurons in vivo. *Nature*, *464*(7293), 1307–1312. https://doi.org/10.1038/nature08947
14. Larkum, M. (2013). A cellular mechanism for cortical associations: An organizing principle for the cerebral cortex. *Trends in Neurosciences*, *36*(3), 141–151. https://doi.org/10.1016/j.tins.2012.11.006
15. Mrsic-Flogel, T. D., Hofer, S. B., Ohki, K., Reid, R. C., Bonhoeffer, T., & Hübener, M. (2007). Homeostatic Regulation of Eye-Specific Responses in Visual Cortex during Ocular Dominance Plasticity. *Neuron*, *54*(6), 961–972. https://doi.org/10.1016/j.neuron.2007.05.028
16. Ohki, K., & Reid, R. C. (2007). Specificity and randomness in the visual cortex. *Current Opinion in Neurobiology*, *17*(4), 401–407. https://doi.org/10.1016/j.conb.2007.07.007
17. Pachitariu, M., Stringer, C., Dipoppa, M., Schröder, S., Rossi, L. F., Dalgleish, H., Carandini, M., & Harris, K. (2016). Suite2p: beyond 10,000 neurons with standard two-photon microscopy. *BioRxiv*, *July*, 061507. https://doi.org/10.1101/061507
18. Palmer, L. M., Shai, A. S., Reeve, J. E., Anderson, H. L., Paulsen, O., & Larkum, M. E. (2014). NMDA spikes enhance action potential generation during sensory input. *Nature Neuroscience*, *17*(3), 383–390. https://doi.org/10.1038/nn.3646
19. Papadopoulos, P. M., Katz, M. J., & Bruno, G. (2003). NPACI rocks: Tools and techniques for easily deploying manageable linux clusters. *Concurrency and Computation: Practice and Experience*, *15*(7–8), 707–725. https://doi.org/10.1002/cpe.722
20. Park, J., Papoutsi, A., Ash, R. T., Marin, M. A., Poirazi, P., & Smirnakis, S. M. (2019). Contribution of Apical and Basal Dendrites of L2/3 Pyramidal Neurons to Orientation Encoding in Mouse V1. *Nature Comm*, 566588. https://doi.org/https://doi.org/10.1101/566588
21. Poirazi, P., Brannon, T., & Mel, B. W. (2003). Pyramidal neuron as two-layer neural network. *Neuron*, *37*(6), 989–999. https://doi.org/10.1016/S0896-6273(03)00149-1
22. Poirazi, P., & Papoutsi, A. (2020). Illuminating dendritic function with computational models. *Nature Reviews Neuroscience*, *21*(6), 303–321. https://doi.org/10.1038/s41583-020-0301-7
23. Rao, R. P. N., & Ballard, D. H. (1999). Predictive coding in the visual cortex: A functional interpretation of some extra-classical receptive-field effects. *Nature Neuroscience*, *2*(1), 79–87. https://doi.org/10.1038/4580
24. Roth, M. M., Dahmen, J. C., Muir, D. R., Imhof, F., Martini, F. J., & Hofer, S. B. (2015). Thalamic nuclei convey diverse contextual information to layer 1 of visual cortex. *Nature Neuroscience*, *19*(2), 299–307. https://doi.org/10.1038/nn.4197
25. Roth, M. M., Dahmen, J. C., Muir, D. R., Imhof, F., Martini, F. J., & Hofer, S. B. (2016). Thalamic nuclei convey diverse contextual information to layer 1 of visual cortex. *Nature*

Neuroscience, *19*(2), 299–307. https://doi.org/10.1038/nn.4197

26. Schindelin, J., Arganda-Carreras, I., Frise, E., Kaynig, V., Longair, M., Pietzsch, T., Preibisch, S., Rueden, C., Saalfeld, S., Schmid, B., Tinevez, J. Y., White, D. J., Hartenstein, V., Eliceiri, K., Tomancak, P., & Cardona, A. (2012). Fiji: An open-source platform for biological-image analysis. *Nature Methods*, *9*(7), 676–682. https://doi.org/10.1038/nmeth.2019
27. Scholl, B., Tan, A. Y. Y., Corey, J., & Priebe, N. J. (2013). Emergence of Orientation Selectivity in the Mammalian Visual Pathway. *Journal of Neuroscience*, *33*(26), 10616–10624. https://doi.org/10.1523/JNEUROSCI.0404-13.2013
28. Schuz, A., & Palm, G. (1989). Density of Neurons and Synapses. *Journal of Comparative Neurology*, *455*, 442–455.
29. Shai, A. S., Anastassiou, C. A., Larkum, M. E., & Koch, C. (2015). Physiology of Layer 5 Pyramidal Neurons in Mouse Primary Visual Cortex: Coincidence Detection through Bursting. *PLoS Computational Biology*, *11*(3), 1–19. https://doi.org/10.1371/journal.pcbi.1004090
30. Silver, R. A. (2010). Neuronal arithmetic. *Nature Reviews. Neuroscience*, *11*(7), 474–489. https://doi.org/10.1038/nrn2864
31. Simons, D. J., & Chabris, C. F. (1999). Gorillas in our midst: sustained inattentional blindness for dynamic events. *Perception*, *28*(28), 1059–1074.
32. Smith, S. L., Smith, I. T., Branco, T., & Häusser, M. (2013). Dendritic spikes enhance stimulus selectivity in cortical neurons in vivo. *Nature*, *503*(7474), 115–120. https://doi.org/10.1038/nature12600
33. Spruston, N. (2008). Pyramidal neurons: dendritic structure and synaptic integration. *Nature Reviews Neuroscience*, *9*(3), 206–221. https://doi.org/10.1038/nrn2286
34. van Elburg, R. A. J., & van Ooyen, A. (2010). Impact of dendritic size and dendritic topology on burst firing in pyramidal cells. *PLoS Computational Biology*, *6*(5), 1–19. https://doi.org/10.1371/journal.pcbi.1000781

988 **7. Supplementary Information**

Compartment Type	Passive/Active Mechanisms	Synaptic Mechanisms
Soma	Hodgkin/Huxley voltage-gated Na^+ channels Hodgkin/Huxley voltage-gated K^+ channels Muscarinic voltage-gated K^+ channels A-Type voltage-gated K^+ channels T-Type Ca^{++} channels High voltage activated (HVA) Ca^{++} channels Calcium-dependent K^+ channels Active ATP Ca^{++} pumps	$GABA_A$ (background-driven)
Basal Dendrites		AMPA (background-driven) NMDA (background-driven) $GABA_A$ (background-driven) AMPA (stimulus-driven) NMDA (stimulus-driven) $GABA_A$ (stimulus-driven)
Apical Dendrites		

989 ***Supplementary Table 1**. Outline of passive, active and synaptic mechanisms present in the model neuron.*

Conductance (mS/cm^2)	Soma	Apical	Basal
g_{Na}	0.505	0.303	0.303
g_{Kdr}	0.05	$1.5*10^{-3}$	$1.5*10^{-3}$
g_{Km}	$2.8*10^{-3}$	$1.27*10^{-3}$	$1.27*10^{-3}$
g_A	5.4	Diameter ≤ 0.8 µm: 108 Diameter > 0.8 µm: 10.8	Diameter ≤ 0.8 µm: 108 Diameter > 0.8 µm: 10.8
g_T	0.03	x ≤ 260 µm: 0.029*sin(0.009*x+0.88) x > 260µm: 0.012	$0.03+6*10^{-5}*x$
g_{HVA}	$0.05*10^{-3}$	x ≤ 260 µm: $0.049*10^{-3}*\sin(0.009*x+0.88)$ x > 260µm: $0.02*10^{-3}$	$0.05*10^{-3}+10^{-7}*x$
g_{KCa}	$2.1*10^{-3}$	$2.1*10^{-3}$	$2.1*10^{-3}$

990 ***Supplementary Table 2**. Outline of membrane mechanism conductances (not synaptic). Reproduced from* (Park
991 et al., 2019).

992

	Model	Cho et al., 2010
RMP, mV	-79	-78.56 ± 1.34
IR, MΩ	123.6	125.2 ± 8.2
τ, ms	17.3	16 ± 0.7
AP amplitude, mV	66.1	67.8 ± 1.8
AP threshold, mV	-41.8	-37.7 ± 1.3
AHP, mV	17.9	13.3 ± 0.5
P-T time, ms	38.6	55.3 ± 2.7
AP adaptation	1.16	1.18 ± 0.02

993 ***Supplementary Table 3**. Outline of model electrophysiological properties. RMP: resting membrane potential, IR:*
994 *Input Resistance measured at hyperpolarizing current (-0.04 nA), AP: action potential, AHP: after*

hyperpolarization measured at depolarizing current (0.16 nA), P-T peak-trough. Reproduced from (Park et al., 2019).

	Conductance (nS)	τ_1, ms	τ_2, ms
NMDA	1.15	2	30
AMPA	0.84	0.1	2.5
$GABA_A$	1.25	0.2	1.4

Supplementary Table 4. *Outline of synaptic mechanism conductances and time constants. Reproduced from* (Park et al., 2019).

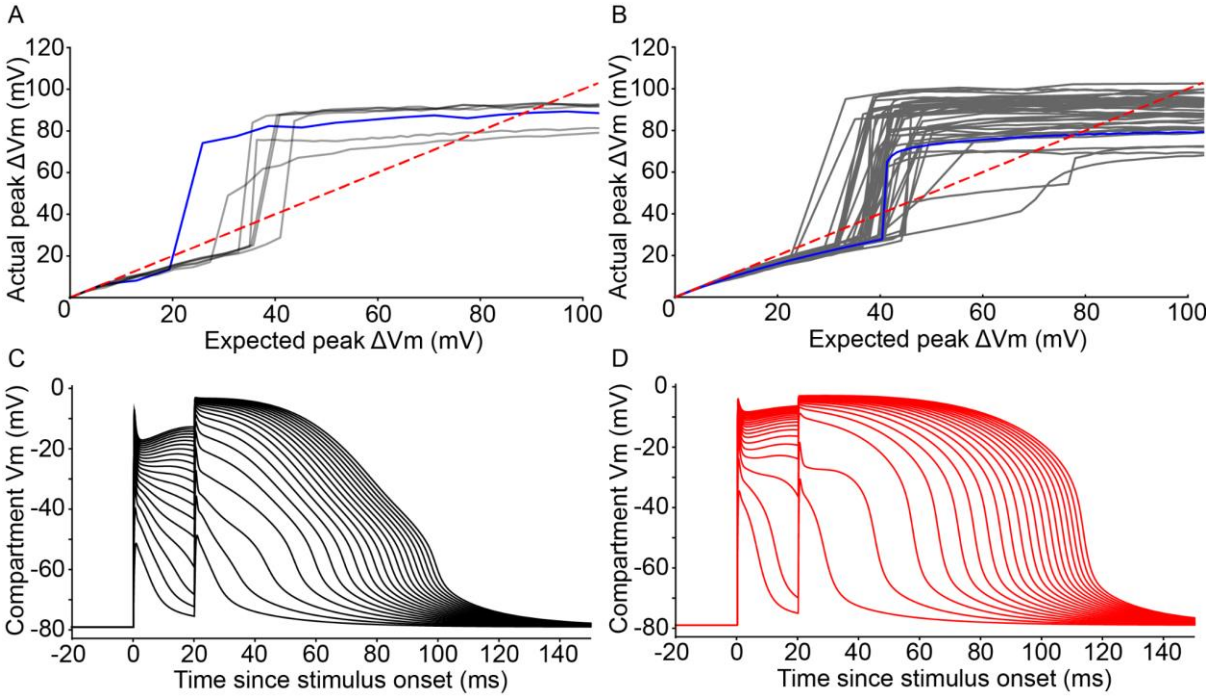

Supplementary Figure 1. *Validation of dendritic non-linear properties. A: Expected vs Actual plot for all basal dendrites undergoing the I3P protocol for 1-200 synapses. Blue line represents the dendrite in Figure 1B (basal dendrite #0). B: Same as A, but for all apical dendrites. Blue line represents dendrite in Figure 1C (apical dendrite #0). C: Example traces from the I3P protocol for NMDA spike generation from basal dendrite #0. Traces are 10 synapses apart from each other. D: Same as C, but for apical dendrite #42 (oblique branch). Dendrites in C and D chosen to show examples of NMDA spiking.*

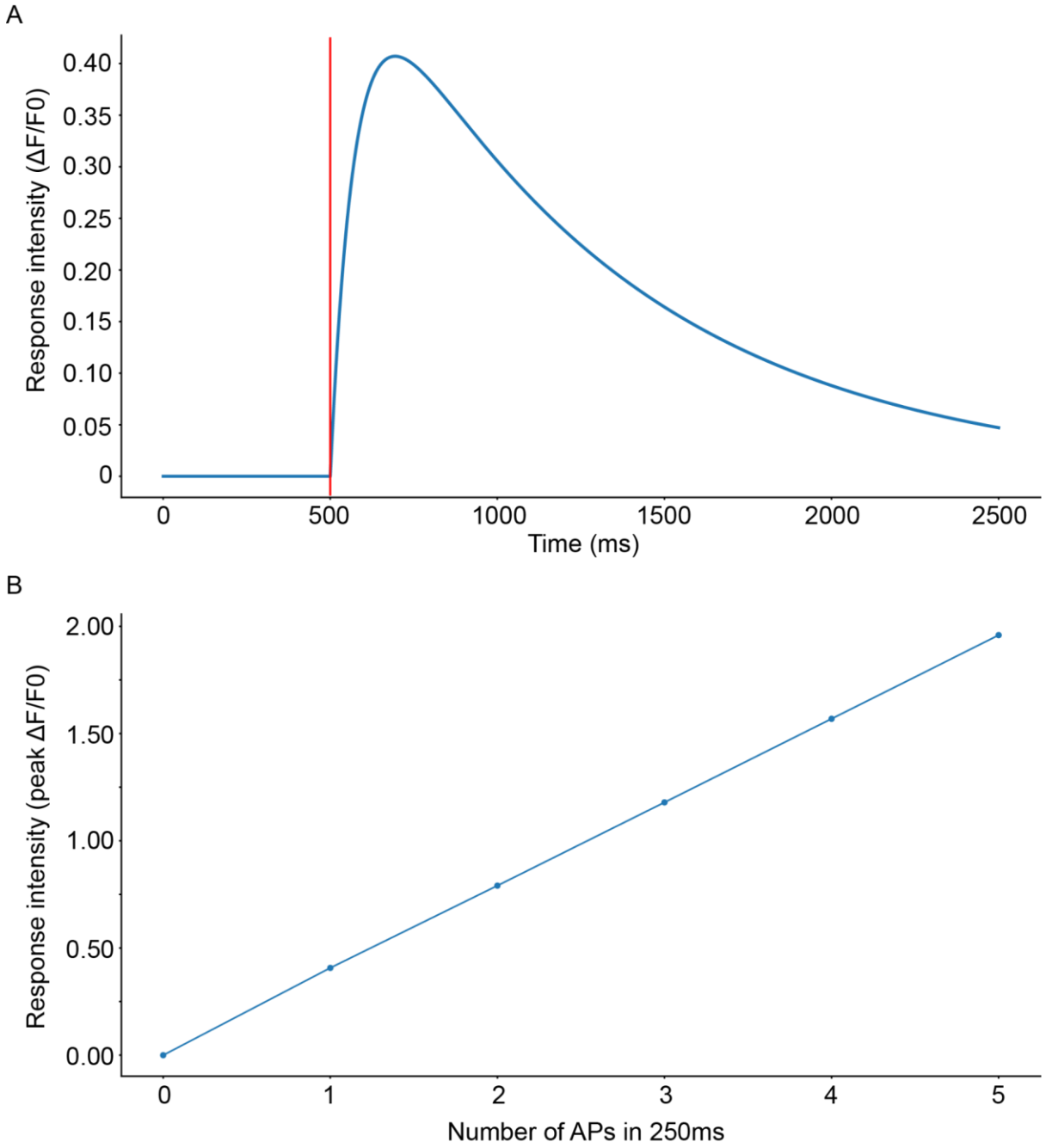

Supplementary Figure 2. *Properties of the GcaMP6s kernel. A: Illustration of the output of the kernel function for a single event (AP) occurring at* t_0 *= 500 ms. (marked as a red line). B: Response intensity as a function of the number of events (APs) within a 250ms window. Compare with* (Chen et al., 2013).

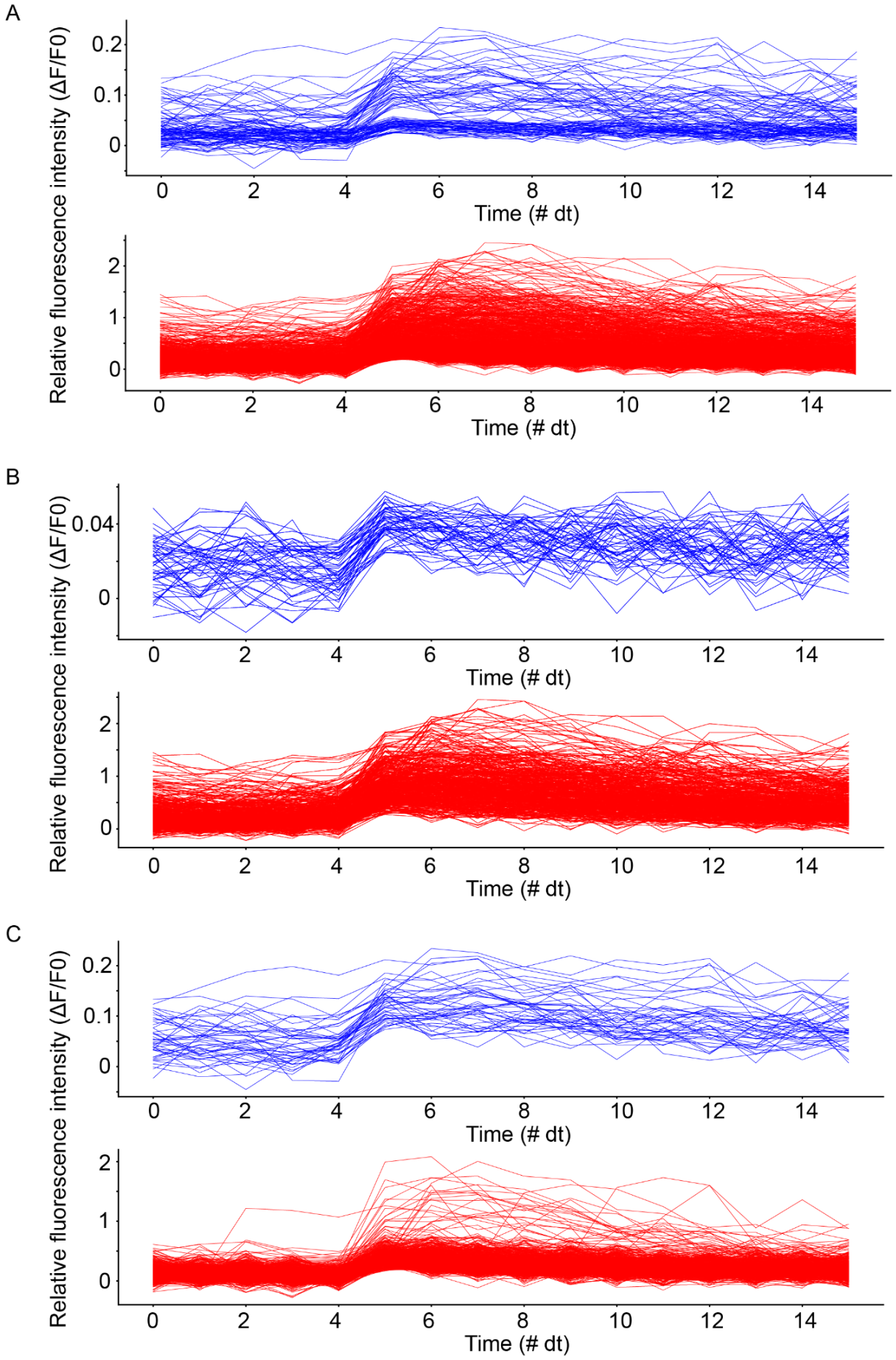
A
Relative fluorescence intensity (ΔF/F0)
0.2
0.1
0
0
2
4
6
8
10
12
14
Time (# dt)
2
1
0
Time (# dt)
B
Relative fluorescence intensity (ΔF/F0)
0.04
0
Time (# dt)
2
1
0
Time (# dt)
C
Relative fluorescence intensity (ΔF/F0)
0.2
0.1
0
Time (# dt)
2
1
0
Time (# dt)

1013

Supplementary Figure 3. *Waveforms of detected calcium fluorescence events. Somatic waveforms in blue, basal dendritic waveforms in red. Spike onset detected at t = 5 dt. A: Waveforms from all detected events from both mice. B: Waveforms from all detected events in mouse 1. C: Waveforms from all detected events from mouse 2. Note: 1 dt is equal to approximately 0.138 s, and exactly equal to the microscope frame time.*

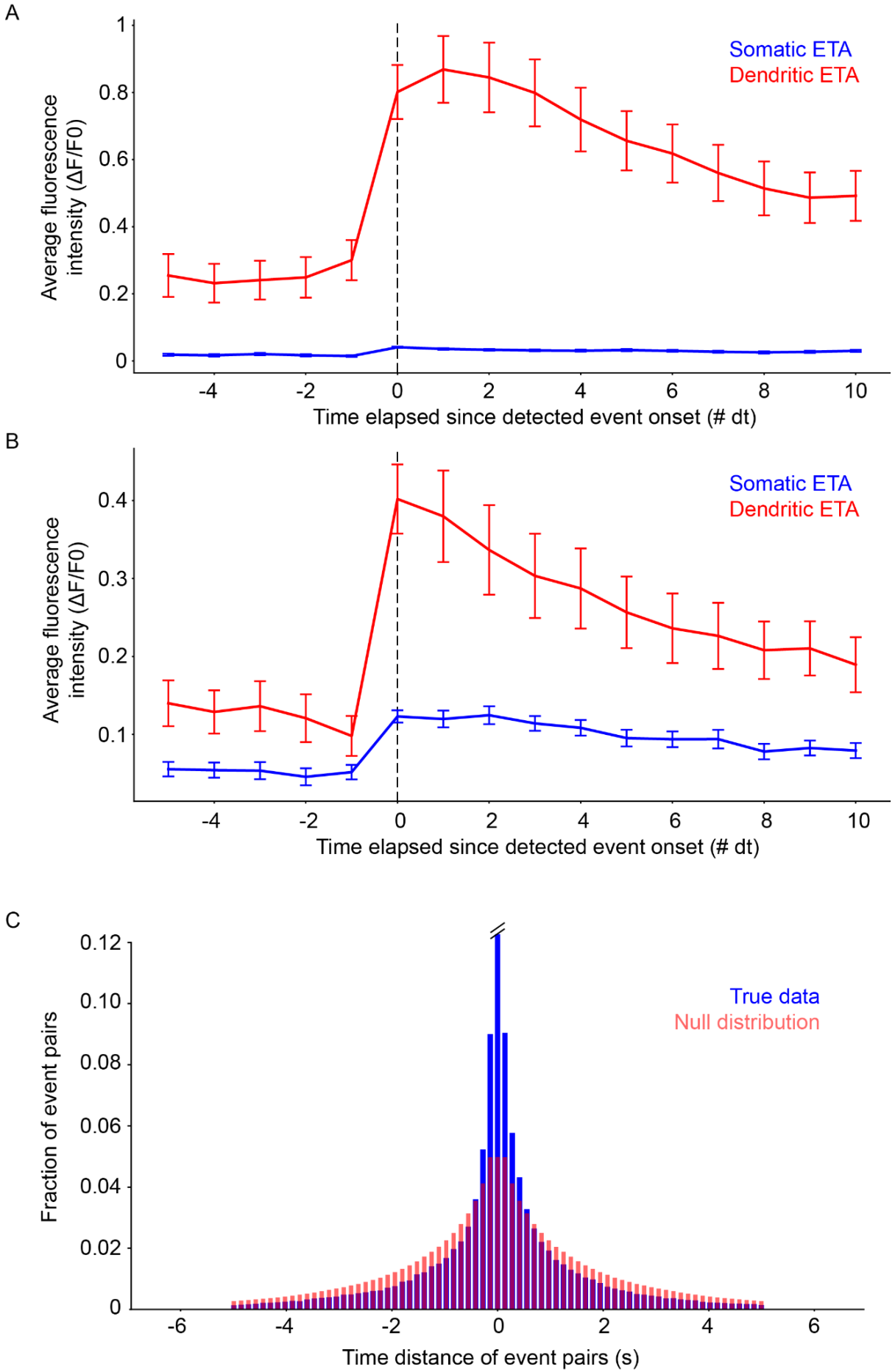
A
Average fluorescence intensity (ΔF/F0)
Somatic ETA
Dendritic ETA
Time elapsed since detected event onset (# dt)
B
Average fluorescence intensity (ΔF/F0)
Somatic ETA
Dendritic ETA
Time elapsed since detected event onset (# dt)
C
Fraction of event pairs
True data
Null distribution
Time distance of event pairs (s)

1019

Supplementary Figure 4. *A: Event-triggered averages for somatic (blue) and basal dendrite (red) events in mouse 1. B: Event-triggered averages for somatic (blue) and basal dendrite (red) events in mouse 2. Note the difference in fluorescence intensity compared to mouse 1. Error bars: Standard error of the mean. C: Comparison of the true (two-photon) data distribution (blue) with the null distribution (light red). Distributions are different (K.S. two-sample test; test value ~0.105, p << 0.05). Note that the middle bar for the true data has been truncated (actual value 0.12267).*

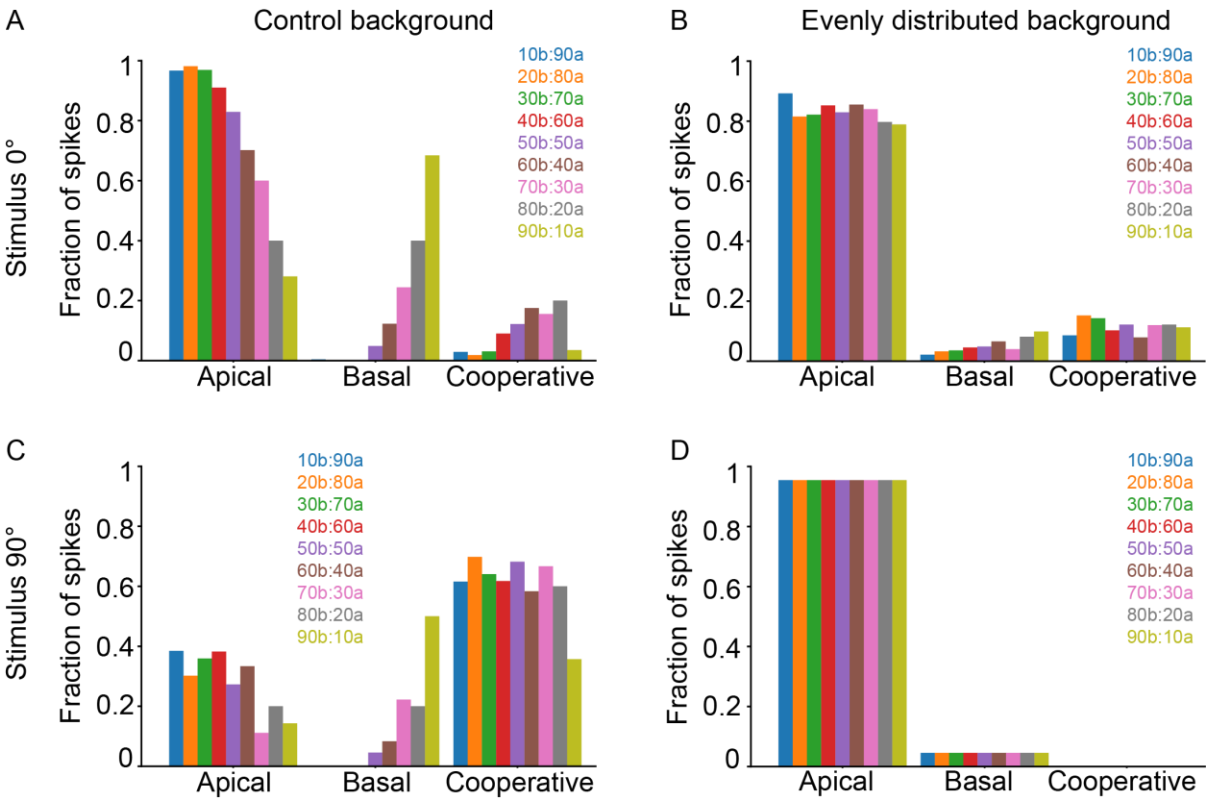

Supplementary Figure 5. *Results of ionic intervention experiments for all synaptic distribution profiles (from [10% basal : 90% apical] to [90% basal : 10% apical]). A: Somatic spike dependence on dendritic sodium conductance when background input distribution follows the same distribution as the stim-driven inputs and the stimulus is set to 0° (preferred orientation). B: Same as A, but background synapses are evenly distributed on both dendritic trees rather than following the same distribution as the stim-driven inputs. C: Same as A, but the stimulus being presented is set to 90° (orthogonal/non-preferred orientation). D: Same as C, but background synapses are evenly distributed on both dendritic trees rather than following the same distribution as the stim-driven inputs. Note how somatic spike dependence on apical sodium conductance decreases when biasing synapse distribution towards the basal tree without ever reaching zero (A, left to right, apical). However, somatic spike dependence on basal sodium conductance decreases and reaches zero when biasing synapse distribution towards the apical tree (A, right to left, basal). A difference is also evident in sodium conductance dependence between stimulus orientations (A vs C), revealing that stimulus-driven spikes do not feature the same dependencies as background-driven spikes. Finally, the role of apical tree sodium conductance is amplified when background-driven synapses are evenly distributed (A vs B and C vs D).*

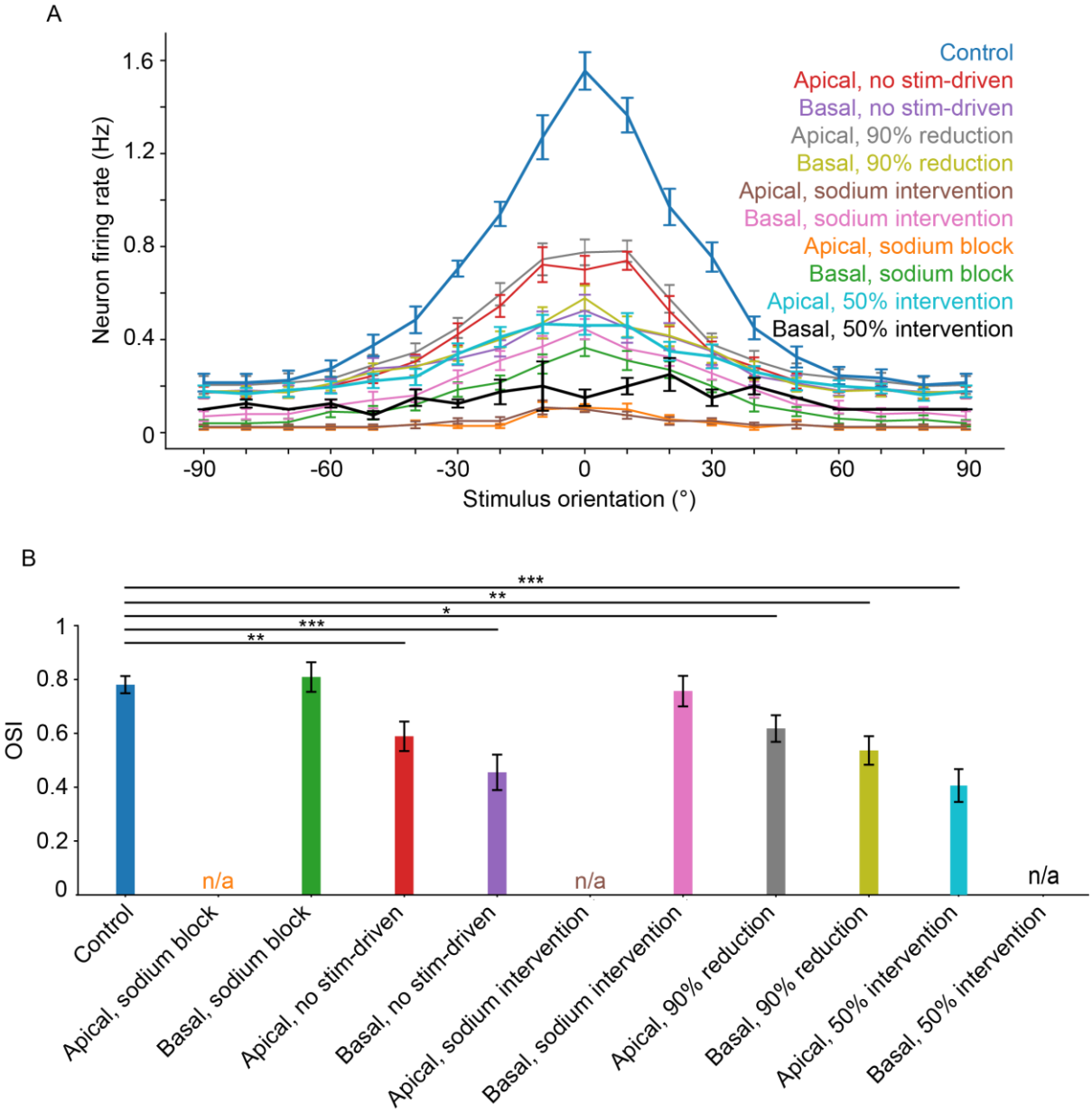

Supplementary Figure 6. *Aggregated results from Figure 5 and other experiments. A: Orientation tuning curves for the control condition and all ionic and synaptic mechanism manipulations. Note that the apical sodium intervention (brown) and apical sodium blockage (orange), as well as the basal 50% (synaptic) intervention (black) curves do not represent adequate orientation tuning. B: OSI values for the control condition and all ionic and synaptic mechanism manipulations. Again, the apical sodium intervention (brown), apical sodium blockage (orange) and basal synaptic intervention (black) curves did not feature adequate tuning, and thus have no OSI values. Stars denote statistical significance at a significance level (α) of 0.05 (*), 0.01 (**) or 0.001 (***), whereas "n.s." stands for "no statistically significant difference", i.e. p-value ≥ α.*